STUDY OF THE FATIGUE LIFE OF STEEL CATENARY RISERS

IN INTERACTION WITH THE SEABED

A Dissertation

by

ALI NAKHAEE

Submitted to the Office of Graduate Studies of
Texas A&M University
in partial fulfillment of the requirement for the degree of

DOCTOR OF PHILOSOPHY

December 2010

Major subject: Ocean Engineering

Study of the Fatigue Life of Steel Catenary Risers in Interaction with the Seabed

STUDY OF THE FATIGUE LIFE OF STEEL CATENARY RISERS

IN INTERACTION WITH THE SEABED

A Dissertation

by

ALI NAKHAEE

Submitted to the Office of Graduate Studies of
Texas A&M University
in partial fulfillment of the requirement for the degree of

DOCTOR OF PHILOSOPHY

Approved by:

Chair of Committee,	Jun Zhang
Committee Members,	Charles Aubeny
	Richard Mercier
	Theofanis Strouboulis
Head of Department,	John Niedzwecki

December 2010

Major subject: Ocean Engineering

ABSTRACT

Study of the Fatigue Life of Steel Catenary Risers in Interaction with the Seabed.

(December 2010)

Ali Nakhaee, B.S., University of Tehran, M.S., University of Tehran

Chair of Advisory Committee: Dr. Jun Zhang

The fatigue life of a Steel Catenary Riser (SCR) near its touch-down zone is substantially affected by its interaction with the seabed. Hence, accurate estimate of its fatigue life requires the understanding and realistic modeling of the interaction between them.

The interaction between SCR and the seabed depends on many factors, such as soil properties, riser characteristics, and the development of trenching at the seafloor. Existing approaches for modeling the seabed in interaction with a SCR approximate the seabed soil by a linear or nonlinear spring and a dashpot which respectively represent the stiffness and damping of the soil. However, they do not take into account certain phenomena resulting from plastic deformation or degradation of the seabed soil, such as trenching. In this study, a more realistic approach is developed for simulating the interaction between a SCR and the seabed soil. In addition to the use of a realistic P-y curve (where P stands for the supporting or resistance force of the seafloor and y for the vertical penetration of the riser into the soil) to simulate the soil deformation during its

interaction with a riser, it considers the development of a trench caused by continuous poundings of a riser on the seabed and then its feedback effect on the variation of the bending moment along the riser.

In this study, it has been found that trenching underneath a SCR may decrease the maximum variation of bending moment near its touch-down zone. Since the variation of the moment dictates the fatigue damage to the SCR, the results based on this approach indicate that the trenching development at the seabed may increase the fatigue life of a SCR and therefore, it may have important application to the design of a SCR.

ACKNOWLEDGEMENTS

TABLE OF CONTENTS

LIST OF FIGURES

Page

LIST OF TABLES

1. INTRODUCTION

1.1. Risers

Risers are one of the essential parts of every hydrocarbon production platform. They are used to convey the fluids between the seabed and the supporting platform during the drilling, injection, completion, production and exporting stages. At the time of drilling, risers are employed to provide transportation of necessary fluids like drilling mud to and from the well. They also support drilling strings, guide tools and auxiliary lines. Production and export risers are used to transfer produced oil and gas to the platform or vessels.

Different riser configurations have been developed to accommodate the requirements for specific floaters and water depths. Top Tension Riser (TTR), Steel Catenary Riser (SCR), Hybrid Riser and Flexible Riser are among the most used type of risers. Figure 1.1 shows some of common configurations of risers. In this study, we will particularly focus on the SCRs. The definition and general concepts about SCRs are discussed later in this dissertation.

_____

This dissertation follows the style of ASCE *Journal of Waterway, Port, Coastal and Ocean Engineering*.

Semisubmersible

FPSO

FPSO

Hybrid Riser

Catenary Riser

Top Tension Riser

Top Tension Riser

Spar

TLP

Semisubmersible

Catenary Riser
with Lazy Wave
configuration

Catenary Riser

Catenary Riser
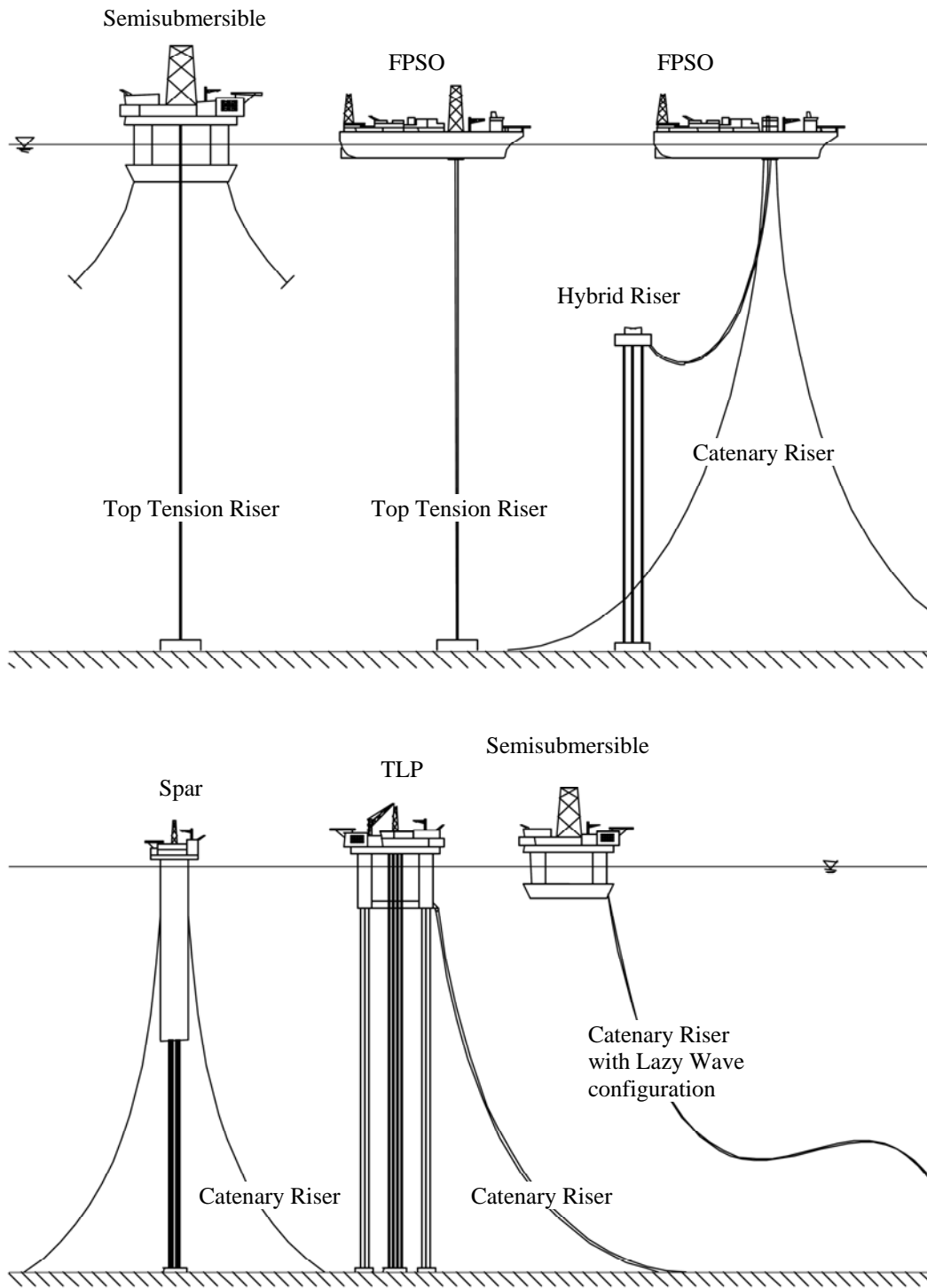
Figure 1.1. Examples of riser configurations (DNV-OS-F201)

1.2. Design of Risers

1.2.1. Loading

The first step in the design of risers is to calculate the loads applied to them. Risers are subjected to various environmental and functonal loads. Some of these loads are as follows (DNV-OS-F201):

- Environmental loads: waves, current and ice

- Floater motions: mean offset, wave frequency motions, and low frequency motions

- Weight and buoyancy of riser and its tubing, coating, marine growth, attachments, and buoyancy modules

- Weight of internal fluid

- Applied tension for Top Tension Risers

- Installation induced residual loads

- Thermal loads

- Drilling operation loadings

- Soil pressure on buried risers

- Soil contact loading in SCRs

- Construction loads

- Pre loading of connectors

- External hydrostatic pressure

- Internal fluid pressure

- Accidental loads

1.2.2. Limit States

The design of riser is based on considering different load combinations. The riser should satisfy the requirements of design for following limit states (DNV-OS-F201):

- *Serviceability Limit State*: It requires that the riser must be able to remain in service and operate properly during normal conditions.

- *Ultimate Limit State*: It requires that the riser must remain intact and avoid rupture, but not necessary be able to operate. This limit state usually corresponds to the maximum resistance to applied loads with 10^{-2} annual exceedence probability.

- *Accidental Limit State*: It is an ultimate limit state due to accidental (infrequent) loads.

- *Fatigue Limit State*: It is an ultimate limit state from accumulated excessive fatigue crack growth or damage under cyclic loading.

The basic procedure required for the fatigue design of the risers is briefly described in next section.

1.3.   Fatigue Life of SCR

Usually in design and analysis of the riser, different loading combinations and limit states should be examined. One of the limit states for which the riser should be carefully analyzed and designed is the Fatigue Limit State. Fatigue is the progressive and localized structural damage that occurs when a material is subjected to the cyclic

loading.

The main method for calculating the fatigue life of the riser is the Miner's rule:

$$\sum \frac{n_i}{N_i} = 1 \qquad \text{(1.1)}$$

where n_i and N_i stand for the number of experienced times of a certain stress level and the number of allowed times of a certain stress level, respectively. N is usually obtained from S-N curves which depend on the material. A typical S-N curve could be seen in Figure 1.2.

Different codes of design and installation of offshore structures, such as API RP2A (American Petroleum Institute, 2001), DNV-RP-F204 (Det Norske Veritas, 2001, 2005 and 2006), and HSE OTO-1999-058 (Home and Safety Executive, 1999) suggest their version of S-N curves for SCRs. For example, the equation for the X' S-N curve proposed by API RP 2A is given in Equation 1.2:

$$N = 2.5 \times 10^{13} \left(SCF \times \Delta\sigma \right)^{-3.74} \quad , \qquad \text{(1.2)}$$

and the equation for the E S-N curve proposed by HSE OTO-1999-058 (Home and Safety Executive, 1999 is as follows:

$$N = 1.04 \times 10^{12} \left(SCF \times \Delta\sigma \right)^{-3} \quad , \qquad \text{(1.3)}$$

where N is the number of allowable loading cycles at a certain stress level, $\Delta\sigma$ is the

stress level, and *SCF* is the stress concentration factor.
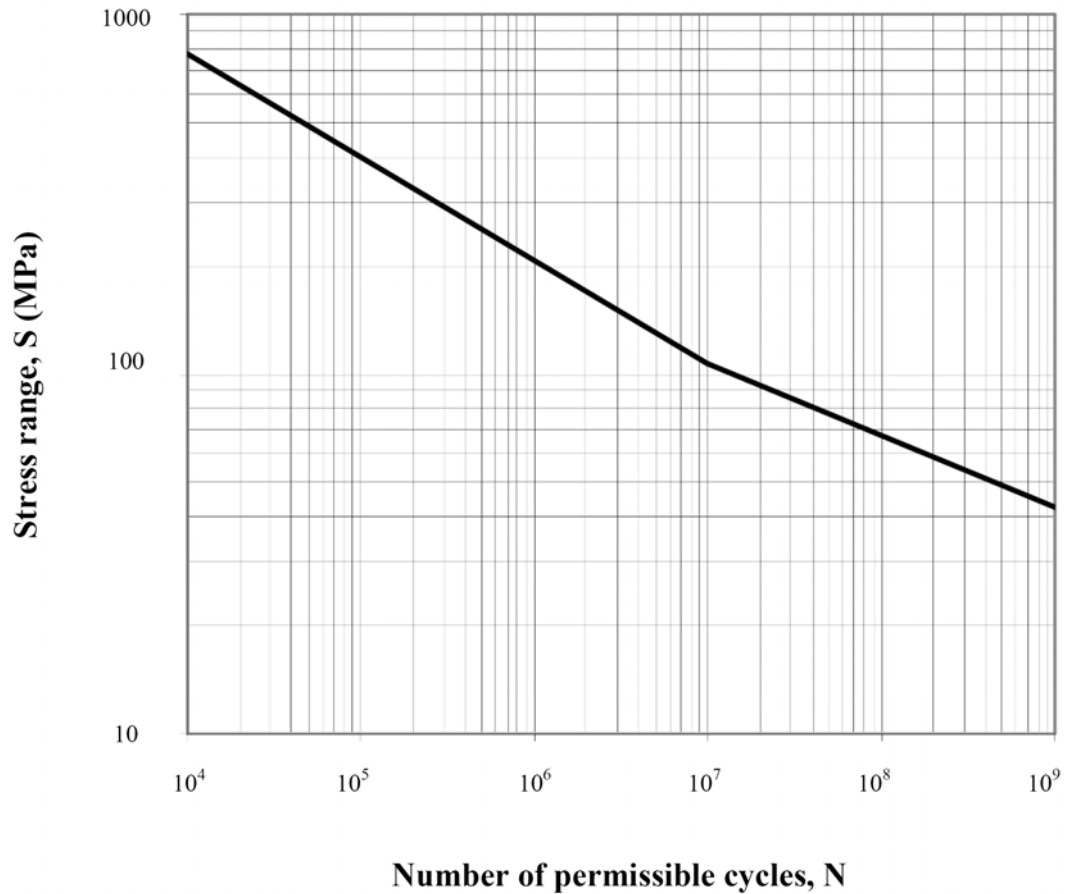
Figure 1.2. Sample of *S-N* curve (from DNV-RP-C203)

Since the SCR experiences many levels of stress during its life, a method for calculating the number of times of each stress level is required. Rainflow method is the most used one. In this study, we assumed that the upper end of the riser experiences a periodic heave or surge motion and hence a simple algorithm is used to determine number of stress levels, *n*.

The main cause of fatigue in the SCR involves the variation of the moment along the riser due to the oscillatory motion of the riser. Studies show that the most vulnerable spots for the fatigue life of a riser are the upper end of the riser where it is attached to the vessel, and the TDZ where it contacts the seabed.

Several methods are employed in order to reduce the fatigue damage in risers. Using flex joints –which consist of one or more metal-elastomer bearings – may reduce the fatigue damage ate upper end of the riser. Particular design of flex joint allows large angular deflections without producing large moments. Figure 1.3 demonstrates a sketch of a SCR and its flex joint. Using flex joints, however, does not have a significant effect on reducing the moments or the variation of moments, which is the main cause of fatigue damage, in the TDZ.
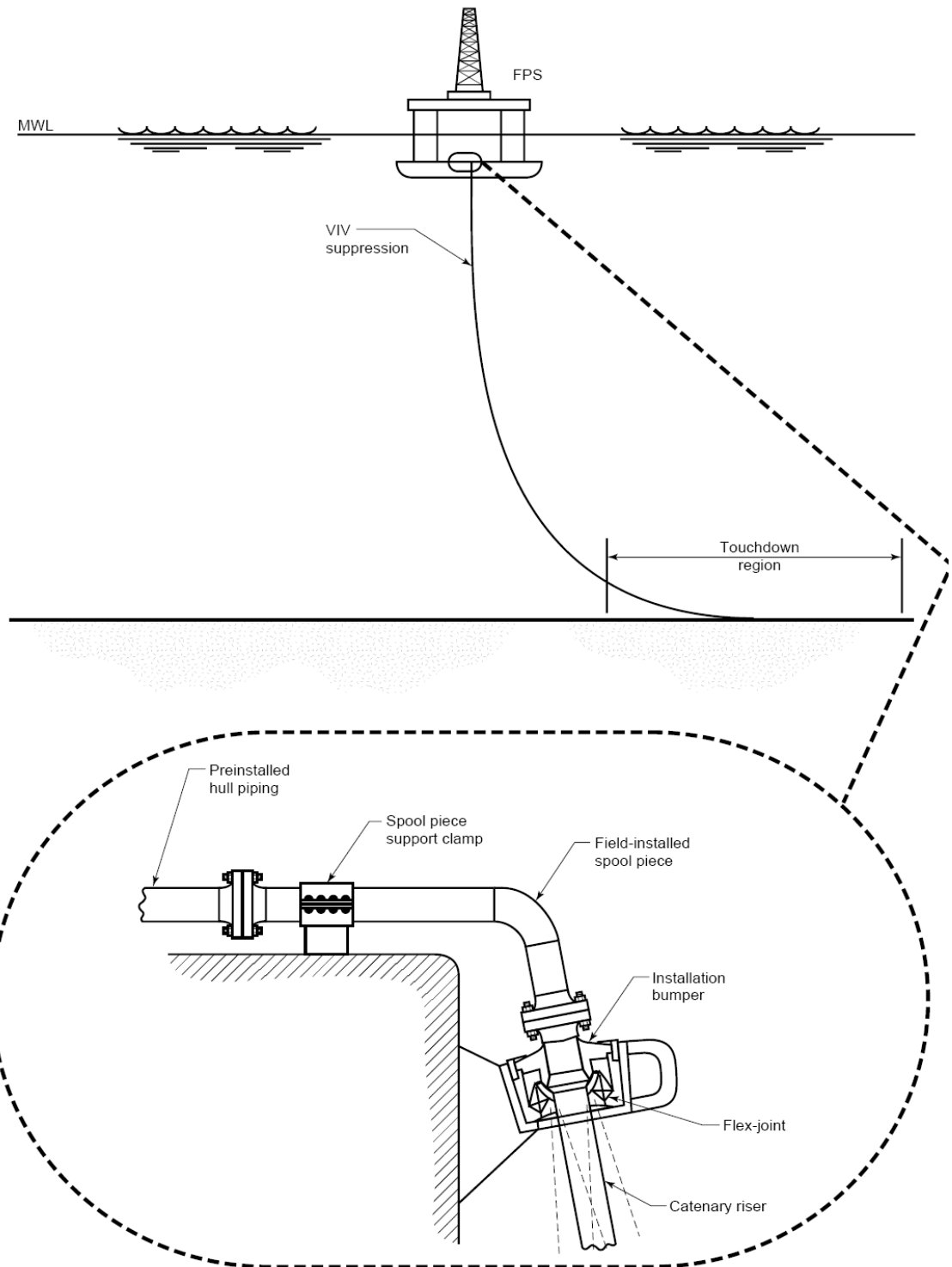
Figure 1.3. Schematic of flex joint (API RP 2RD)

Some studies show that the Fatigue damage at the TDZ is usually more severe than other zones of a SCR (Xu et al., 2006). Various solutions have been suggested to increase the fatigue life of the SCR in its TDZ:

- Change in the SCR configurations: upper end angle, and draft
- Using coating or buoyancy units for lightening the TDZ
- Using more resistant material in the TDZ: titanium or composite
- Lazy wave configuration

Bhat et al. (2004) and Aggarwal et al. (2005) give a brief description of these methods and their possible effect on the improvement of the fatigue life of the riser.

1.4.   Riser-Soil Interaction Modeling

The model used for analyzing the seabed behavior has a large effect on the calculated fatigue life of the SCR. For example, changing the value of the soil stiffness in the model may result in drastic change in the fatigue damage. Bridge et al. (2004) suggest that for a certain cae study (STRIDE JIP), changing the soil stiffness from infinity (rigid seabed) to a small value (100 kN/m/m), will increase the predicted fatigue life for 120%.

Existing approaches for modeling the seabed in interaction with a SCR approximate the behavior of the seabed soil by linear or nonlinear spring and dashpot which respectively represent the stiffness and damping of the soil. These models are

considered to be too simplified to account for certain phenomena resulting from the plastic deformation of soil, such as trenching development at the seabed (Leira et al., 2004).

This study extends an existing code for the dynamic analysis of risers and mooring lines, CABLE3D, to allow for a more realistic behavior of the seabed soil in contact with the riser including the development of trenching at the seabed. A degradation P-y curve presented by Aubeny et al. 92006) and Aubeny and Biscontin (2008, 2009) is used to determine the rate of trench development at the seabed near the TDZ of a SCR experiencing forced periodic heave and surge at its upper end. The trenching development at the seabed is then considered in the computation of the bending moment along a riser, especially near its TDZ. The details of the CABLE3D and the soil-interaction model are described in Sections 2-4.

2. CABLE3D

2.1. Introduction

CABLE3D is a FORTRAN code for computing dynamics of the mooring/riser system attached to a floating structure. A nonlinear Finite Element Method is used to solve the governing equations of a slender-body (Ma and Webster, 1994). There are two different elements in the CABLE3D. First, BEAM element with infinitesimal elongation and considering bending stiffness. Second, BAR element with no bending stiffness and large-elongation assumption to accommodate the characteristics of elements such as springs and polyester ropes that are often used in model tests and mooring systems. The equations in this chapter are derived and explained in details by Chen (2002).

The dynamic equations for small extensible beam with bending stiffness are presented (Chen et al., 2001).Then the Galerkin's method is used to discretize the dynamic equations in space, resulting into a set of nonlinear 2nd-order ordinary differential equations in the time domain. Finally a Newmark-β method was employed for time-domain integration of the discretized equations.

2.2. Equation of Motion

In a 3-D Cartesian coordinate system, the instantaneous configuration of a rod is expressed in terms of a vector, $\boldsymbol{r}$ (s,t), which is a function of s, the deformed arc length along the rod, and time t (Figure 2.1). In Figure 2.1, $\boldsymbol{t}, \boldsymbol{n}$ and $\boldsymbol{b}$ are unit vectors in

tangential, normal and binormal directions, respectively, and $\mathbf{e}_x$ ($\mathbf{e}_1$), $\mathbf{e}_y$ ($\mathbf{e}_2$) and $\mathbf{e}_z$ ($\mathbf{e}_3$)

are unit vectors in the x-, y- and z-axis, respectively. If we assume that the rod is

inextensible, i.e., arc length s is the same in both deformed and undeformed states.

The internal state of stress at a point on the rod is described fully by the resultant

force $\mathbf{F}$ and the resultant moment $\tilde{\mathbf{M}}$ acting at the centerline of the rod. On the basis of

conservation of linear momentum and moment of momentum, we have equations 2.1

and 2.2:

$$\mathbf{F}' + \mathbf{q} = \rho \ddot{\mathbf{r}}(s,t) \tag{2.1}$$

$$\tilde{\mathbf{M}}' + \mathbf{r}' \times \mathbf{F} + \mathbf{m} = 0 \tag{2.2}$$

where $\mathbf{q}$ is the distributed external force per unit length, ρ is the mass per unit length, $\mathbf{m}$

is the external moment per unit length, and a superposed dot denotes differentiation with

respect to time. The prime denotes the derivatives with respect to s. In above equations,

the effects of rotary inertia and shear deformations are neglected.
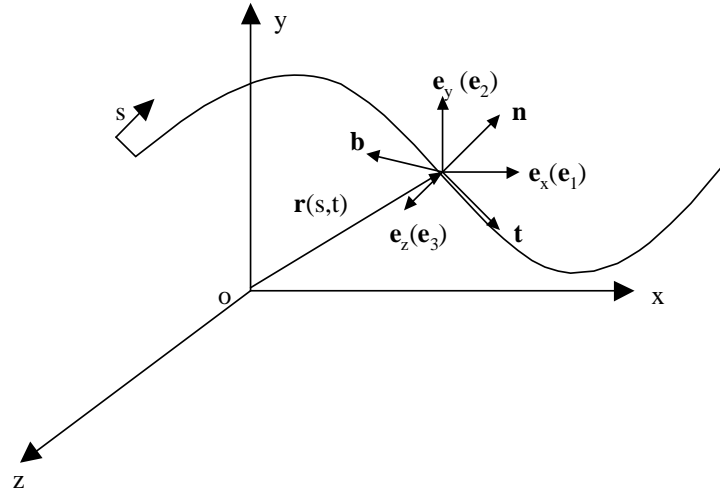
Figure 2.1. Coordinate system

For a elastic rod with equal principal stiffness, the bending moment is proportional to curvature and directed along the binormal according to the Bernoulli-Euler theory. In addition, the torsional component H is proportional to the angle of twist per unit length and is directed along the tangent. The resultant moment $\tilde{\mathbf{M}}$ can be written as:

$$\tilde{\mathbf{M}} = \mathbf{r}' \times (B\mathbf{r}'') + H\mathbf{r}' \tag{2.3}$$

$$\tilde{\mathbf{M}}' = \mathbf{r}' \times (B\mathbf{r}'')' + H'\mathbf{r}' + H\mathbf{r}'' \tag{2.4}$$

where H is the torque and B is the bending rigidity. Assuming $H=0$ and $\mathbf{m}=0$, (no torsion or external moment) and plug $\tilde{\mathbf{M}}'$ into equation 2.2, equations 2.1 and 2.2 reduced to the expression of $\mathbf{F}$:

$$\mathbf{F} = \lambda \mathbf{r}' - (B\mathbf{r}'')' \tag{2.5}$$

$$\lambda = T - B\kappa^2 \tag{2.6}$$

where $\kappa^2 = -\mathbf{r}'\cdot\mathbf{r}'''$, κ is the local curvature of the rod, and $T(s,t) = \mathbf{r}'\cdot\mathbf{F}$ is the local tension. In the derivation the assumption of the inextensibility condition was made:

$$\mathbf{r}'\cdot\mathbf{r}' = 1 \tag{2.7}$$

The equation of motion is finally derived by plugging $\mathbf{F}$ of equation 2.5 into equation 2.1:

$$-(B\mathbf{r}'')'' + (\lambda\mathbf{r}')' + \mathbf{q} = \rho\ddot{\mathbf{r}} \tag{2.8}$$

Equation 2.7 can be expanded to allow for small extension by:

$$\mathbf{r}'\cdot\mathbf{r}' = (1+\varepsilon)^2 \tag{2.9}$$

where $\varepsilon = T/EA$, EA is the elastic stiffness of the rod. When ε is very small, equation of motion (2.8) and equation of Lagrange multiplier λ (2.6) are valid.

The external forces applied on a rod consist of gravity forces, hydrostatic and hydrodynamic forces. The gravity force on the rod leads to a distributed load given by:

$$\mathbf{q}_t(s,t) = -\rho_t g A_t \mathbf{e}_y \tag{2.10}$$

The hydrodynamic forces acting on the rod consist of added-mass force, drag force, and Froude-Krylov force. The Morrison equation is used to predict the first two terms:

$$\mathbf{q}_f^I(s,t) = \rho_f A_f C_{Mn} \mathbf{N}(\mathbf{a}_f - \ddot{\mathbf{r}}) + \rho_f A_f C_{Mt} \mathbf{T}(\mathbf{a}_f - \ddot{\mathbf{r}}) \tag{2.11}$$

$$\begin{aligned}
\mathbf{q}_f^D(s,t) = {} & \frac{1}{2}\rho_f D_f C_{Dn} \mathbf{N}(\mathbf{v}_f - \dot{\mathbf{r}})\left|\mathbf{N}(\mathbf{v}_f - \dot{\mathbf{r}})\right| \\
& + \frac{1}{2}\rho_f D_f C_{Dt} \mathbf{T}(\mathbf{v}_f - \dot{\mathbf{r}})\left|\mathbf{T}(\mathbf{v}_f - \dot{\mathbf{r}})\right|
\end{aligned} \tag{2.12}$$

where C_{Mn}, C_{Mt}, C_{Dn} and C_{Dt} are the normal added-mass coefficient, tangential added-mass coefficient, normal drag coefficient and tangential drag coefficient respectively.

Froude - Krylov force due to sea water outside the rod is:

$$\mathbf{q}_f^{F-K}(s,t) = \rho_f(g\mathbf{e}_y + \mathbf{a}_f)A_f + (P_f A_f \mathbf{r}')' \tag{2.13}$$

Froude-Krylov force (pressure forces) due to the fluid inside the rod is:

$$\mathbf{q}_i^{F-K}(s,t) = -\rho_i g A_i \mathbf{e}_y - (P_i A_i \mathbf{r}')' \tag{2.14}$$

in the above equations:

$\rho = \rho_t A_t + \rho_i A_i$, the mass per unit rod (including the internal fluid),

$\rho_f(s) = $ the mass density of the sea water,

$\rho_i(s) = $ the mass density of the inside fluid,

$\rho_t(s) = $ the mass density of the tube,

$A_f(s)$ = the outer cross-section area of the rod,

$D_f(s)$ = the diameter of the rod,

$A_i(s)$ = the inner cross-section area of the rod,

$A_t(s)$ = the structural cross-section area of the rod,

$\mathbf{v}_f$ = the velocity of the sea water (current and wave),

$\mathbf{a}_f$ = the acceleration of the sea water (current and wave),

P_f = pressure of the sea water,

P_i = pressure of the internal fluid,

$\mathbf{T}, \mathbf{N}$ = transfer matrices,

$\mathbf{I}$ = identity matrix,

where the subscripts f, i and t denote the sea water, the fluid inside the tube and the tube itself. $\mathbf{T}$ and $\mathbf{N}$ are defined by:

$$\mathbf{T} = \mathbf{r}'^T \mathbf{r}' \tag{2.15}$$

$$\mathbf{N} = \mathbf{I} - \mathbf{T} \tag{2.16}$$

The governing equation is finally obtained as:

$$\mathbf{M}\ddot{\mathbf{r}} + (B\mathbf{r}'')'' - (\tilde{\lambda}\mathbf{r}')' = \mathbf{q} \tag{2.17}$$

where

$$\mathbf{q} = (\rho_f A_f - \rho_i A_i - \rho_t A_t) g \, \mathbf{e}_y + \rho_f A_f (\mathbf{I} + C_{Mn} \mathbf{N} + C_{Mt} \mathbf{T}) \mathbf{a}_f$$
$$+ \frac{1}{2} \rho_f D_f C_{Dn} \mathbf{N}(\mathbf{v}_f - \dot{\mathbf{r}}) \left| \mathbf{N}(\mathbf{v}_f - \dot{\mathbf{r}}) \right| \tag{2.18}$$
$$+ \frac{1}{2} \rho_f D_f C_{Dt} \mathbf{T}(\mathbf{v}_f - \dot{\mathbf{r}}) \left| \mathbf{T}(\mathbf{v}_f - \dot{\mathbf{r}}) \right|$$

The virtual mass matrix:

$$\mathbf{M} = (\rho_t A_t + \rho_i A_i) \mathbf{I} + \rho_f A_f C_{Mn} \mathbf{N} + \rho_f A_f C_{Mt} \mathbf{T} \tag{2.19}$$

$$\tilde{\lambda} = (T + P_f A_f - P_i A_i) - B\kappa^2 \tag{2.20}$$

and assume curvature κ is small, then ε can expressed as:

$$\varepsilon = \frac{T}{EA} \approx \frac{\tilde{\lambda} - P_f A_f + P_i A_i}{EA} \tag{2.21}$$

The term in the parentheses in equation 2.20 is known as the "effective tension".

2.3.   Numerical Implementation

2.3.1.   Finite Element Model

The motion equation and constraint condition for a rod of small elongation are summarized in equations 2.9 and 2.17.

The procedure for numerical implementation for the equations of small elongation element is described here. The Galerkin's method is used to discretize the partial differential equations of motion for (2.17) and the constraint equation (2.9) in space,

resulting in a set of nonlinear 2nd-order ordinary differential equations in the time

domain.

Two types of shape functions are used. Hermite cubics a (s) for describing the

shape of the rod and quadratics $p(s)$ for the parameters of $\tilde{\lambda}$, B, $\mathbf{q}$, $\mathbf{M}$, etc. The Hermite

cubic shape function $a(s)$ are:

$$
\begin{aligned}
a_1(\xi) &= 1 - 3\xi^2 + 2\xi^3 \\
a_2(\xi) &= \xi - 2\xi^2 + \xi^3 \\
a_3(\xi) &= 3\xi^2 - 2\xi^3 \\
a_4(\xi) &= -\xi^2 + \xi^3
\end{aligned}
\tag{2.22}
$$

and the quadratic shape function $p(s)$ are:

$$
\begin{aligned}
p_1(\xi) &= 1 - 3\xi + 2\xi^2 \\
p_2(\xi) &= 4\xi(1-\xi) \\
p_3(\xi) &= \xi(2\xi - 1)
\end{aligned}
\tag{2.23}
$$

where ξ is a nondimensional coordinate given by $\xi = s/L$, L is the unstretched length of

the element. Therefore, the position of the rod in the inertia coordinate system, the

Lagrange multiplier $\tilde{\lambda}$, the distributed loading and the mass matrix are approximated as

(tensor summation rule is employed):

$$\mathbf{r}(s,t) = u_{in}(t)a_i(s)\mathbf{e}_n$$
$$\tilde{\lambda}(s,t) = \tilde{\lambda}_m(t)p_m(s)$$
$$B(s) = B_m p_m(s) \tag{2.24}$$
$$\mathbf{q}(s,t) = q_{mn}(t)p_m(s)\mathbf{e}_n$$
$$\mathbf{M}(s,t) = \mathbf{M}_m(t)p_m(s)$$

where $n = 1 - 3$, $i = 1 - 4$ and $m = 1 - 3$. With the special selection of the shape functions

the coefficients in the summation (2.42) are given by:

$$u_{1n}(t) = \mathbf{r}_n(0,t)$$
$$u_{2n}(t) = L\mathbf{r'}_n(0,t)$$
$$u_{3n}(t) = \mathbf{r}_n(L,t) \tag{2.25}$$
$$u_{4n}(t) = L\mathbf{r'}_n(L,t)$$

$$\tilde{\lambda}_1(t) = \tilde{\lambda}(0,t)$$
$$\tilde{\lambda}_2(t) = \tilde{\lambda}(L/2,t) \tag{2.26}$$
$$\tilde{\lambda}_3(t) = \tilde{\lambda}(L,t)$$

$$B_1 = B(0)$$
$$B_2 = B(L/2) \tag{2.27}$$
$$B_3 = B(L)$$

$$\mathbf{q}_1(t) = \mathbf{q}(0,t)$$
$$\mathbf{q}_2(t) = \mathbf{q}(L/2,t) \tag{2.28}$$
$$\mathbf{q}_3(t) = \mathbf{q}(L,t)$$

and

$$\mathbf{M}_1(t) = \mathbf{M}(0,t)$$
$$\mathbf{M}_2(t) = \mathbf{M}(L/2,t) \qquad\qquad\qquad \textbf{(2.29)}$$
$$\mathbf{M}_3(t) = \mathbf{M}(L,t)$$

$$\mathbf{M}_m = \left\{ \begin{matrix} M_{11} & M_{12} & M_{13} \\ M_{21} & M_{22} & M_{23} \\ M_{31} & M_{32} & M_{33} \end{matrix} \right\}_m \qquad\qquad \textbf{(2.30)}$$

To discretize the governing equation, we rewrite equation (2.19) as follows:

$$\mathbf{M\ddot{r}} + (B\mathbf{r}'')'' - (\tilde{\lambda}\mathbf{r}')' - \mathbf{q} = 0 \qquad\qquad \textbf{(2.31)}$$

Equation 2.31 may be reduced to a set of ordinary differential equations using Galerkin's method. Multiplying both side of the equation with $a_i(s)$ and integrating it with respect to s from 0 to L for an element of the rod with length of L:

$$\int_0^L \left\{ \mathbf{M\ddot{r}} + (B\mathbf{r}'')'' - (\tilde{\lambda}\mathbf{r}')' - \mathbf{q} \right\} a_i(s)\, ds = 0 \qquad\qquad \textbf{(2.32)}$$

Integrating the above equation by parts results in equation 2.33:

$$\int_0^L \left\{ \mathbf{M\ddot{r}} + (B\mathbf{r}'')'' - (\tilde{\lambda}\mathbf{r}')' - \mathbf{q} \right\} a_i(s)\, ds = 0 \qquad\qquad \textbf{(2.33)}$$

or,

$$\int_0^L \left\{ \mathbf{M}\ddot{\mathbf{r}}a_i(s) + B\mathbf{r}''a_i''(s) + \tilde{\lambda}\mathbf{r}'a_i'(s) - \mathbf{q}\,a_i(s) \right\} ds$$

$$= B\mathbf{r}''\,a_i'(s)\Big|_o^L + \left\{ \tilde{\lambda}\mathbf{r}' - (B\mathbf{r}'')' \right\} a_i(s)\Big|_0^L \tag{2.34}$$

The first term on the right-hand side of the equation is related to the moments at the ends of the element, and the second term (in curly brackets) is the forces at the ends of the element. The right-hand side terms are called generalized forces $\mathbf{f}_i$, which can be expressed as:

$$\mathbf{f}_i = B\mathbf{r}''\,a'_i\Big|_o^L + \left\{ \tilde{\lambda}\mathbf{r}' - (B\mathbf{r}'')' \right\} a_i\Big|_0^L \quad , i = 1,2,3,4 \tag{2.35}$$

$$\mathbf{f}_1 = -\left\{ \tilde{\lambda}\mathbf{r}'(0) - (B\mathbf{r}'')'(0) \right\} = -\mathbf{F}(0) \tag{2.36}$$

$$\mathbf{f}_2 = -\frac{1}{L}B\mathbf{r}''(0) = \frac{1}{L}\mathbf{r}'(0) \times \tilde{\mathbf{M}}(0) \tag{2.37}$$

$$\mathbf{f}_3 = \left\{ \tilde{\lambda}\mathbf{r}'(L) - (B\mathbf{r}'')'(L) \right\} = \mathbf{F}(L) \tag{2.38}$$

$$\mathbf{f}_4 = \frac{1}{L}B\mathbf{r}''(0) = -\frac{1}{L}\mathbf{r}'(L) \times \tilde{\mathbf{M}}(L) \tag{2.39}$$

Inserting the expression (2.24) and the shape functions (2.22) and (2.23) into (2.34), we obtain the following set of ordinary differential equations for a small elongation element with prescribed bending stiffness:

$$\gamma_{ikm} M_{njm} \ddot{u}_{kj} + \alpha_{ikm} B_m u_{kn} + \beta_{ikm} \tilde{\lambda}_m u_{kn} = \mu_{im} q_{mn} + f_{in} \qquad \textbf{(2.40)}$$

Similarly, we obtain the discretized form of the constraint equation (2.9):

$$\frac{1}{2}\beta_{ikm} u_{in} u_{kn} = \frac{1}{2}\left\{\tau_m + 2\eta_{lm}\varepsilon_l + \tilde{\gamma}_{jlm}\varepsilon_j\varepsilon_l\right\} \qquad \textbf{(2.41)}$$

where the summation algorithm is employed. i and k run from 1 to 4; j, l, m and n runs from 1 to 3; and

$$\alpha_{ikm} = \frac{1}{L^3}\int_0^1 a_i''(\xi)a_k''(\xi)p_m(\xi)d\xi$$

$$\beta_{ikm} = \frac{1}{L}\int_0^1 a_i'(\xi)a_k'(\xi)p_m(\xi)d\xi$$

$$\gamma_{ikm} = L\int_0^1 a_i(\xi)a_k(\xi)p_m(\xi)d\xi$$

$$\mu_{im} = L\int_0^1 a_i(\xi)p_m(\xi)d\xi \qquad \textbf{(2.42)}$$

$$\tau_m = L\int_0^1 p_m(\xi)d\xi$$

$$\eta_{lm} = L\int_0^1 p_l(\xi)p_m(\xi)d\xi$$

$$\tilde{\gamma}_{ikm} = L\int_0^1 p_j(\xi)p_l(\xi)p_m(\xi)d\xi$$

In equation 2.40, f_{in} is the generalized internal forces at the two ends of an element. For two smoothly connected elements (n) and ($n+1$), the continuity of a rod yields:

$$^{(n)}u_{3n} = {}^{(n+1)}u_{1n}$$
$$^{(n)}u_{4n} / L^{(n)} = {}^{(n+1)}u_{2n} / L^{(n+1)}$$
$$^{(n)}\tilde{\lambda}_3 = {}^{(n+1)}\tilde{\lambda}_1$$

(2.43)

where $L^{(n)}$ and $L^{(n+1)}$ are the length of (n) and $(n+1)$ elements respectively. If no

concentrated mass, forces and moments are applied at the node connecting two elements,

then the generalized internal forces cancel out when two adjacent elements connected.

This condition can be written as:

$$^{(n)}\mathbf{f}_3 + {}^{(n+1)}\mathbf{f}_1 = 0$$
$$^{(n)}\mathbf{f}_4 L^{(n)} + {}^{(n+1)}\mathbf{f}_2 L^{(n+1)} = 0$$

(2.44)

At free ends of the first and last elements, it is necessary to supply the boundary

conditions, such as, hinged boundary conditions. If N elements are used to describe a

line in three dimensions, then the procedure results in 15+8(N-1) independent equations

and coefficients.

2.3.2. Static Problem

For a static problem, all the terms related to the time derivatives are zero.

Therefore, equation 2.40 is reduced to:

$$\alpha_{ikm} B_m u_{kn} + \beta_{ikm} \tilde{\lambda}_m u_{kn} = \mu_{im} q_{mn} + f_{in}$$

(2.45)

The Newton's method is employed to solve the nonlinear equations. Let u^0 and λ^0

a first guess, then the updated values of u and λ are:

$$u_{kn} = u_{kn}^0 + \delta u_{kn}$$
$$\tilde{\lambda}_m = \tilde{\lambda}_m^0 + \delta \tilde{\lambda}_m$$

(2.46)

Plugging the new expression of u and $\tilde{\lambda}$ into Equation (2.45) and discarding all the high order terms, the static problem is then represented by the following equations for small elongation elements.

$$(\alpha_{ikm} B_m + \beta_{ikm} \tilde{\lambda}_m^0) \delta u_{kn} + \beta_{ikm} u_{kn}^0 \delta \tilde{\lambda}_m$$
$$= \mu_{im} q_m - \alpha_{ikm} B_m u_{kn}^0 - \beta_{ikm} \tilde{\lambda}_m^0 u_{kn}^0 + f_{in}$$

(2.47)

$$\beta_{ikm} u_{in}^0 \delta u_{kn} - (\eta_{\lim} + \tilde{\gamma}_{jlk} \varepsilon_j^0) \left\{ \frac{\delta \tilde{\lambda}}{EA} + (\rho_f A_f - \rho_i A_i) g \frac{\delta y}{EA} \right\} \Bigg|_l$$
$$= \frac{1}{2} (\tau_m + 2\eta_{lm} \varepsilon_l^0 + \tilde{\gamma}_{jlm} \varepsilon_j^0 \varepsilon_l^0 - \beta_{ikm} u_{in}^0 u_{kn}^0)$$

(2.48)

where

$$\delta y_1 = \delta u_{12}$$
$$\delta y_2 = 0.5 \delta u_{12} + 0.125 \delta u_{22} + 0.5 \delta u_{32} - 0.125 \delta u_{42}$$
$$\delta y_3 = \delta u_{32}$$

(2.49)

Equations (2.47) and (2.48) are written in a matrix form $\mathbf{a}\delta\mathbf{x}=\mathbf{b}$ for each element, where the unknown vector $\delta\mathbf{x}$ consisting of the 15 unknowns mentioned above is defined

as:

$$\delta\mathbf{x} = (\delta u_{11},\ \delta u_{12},\ \delta u_{13},\ \delta u_{21},\ \delta u_{22},\ \delta u_{23},\ \delta\lambda_1,\ \delta\lambda_2,\ \delta u_{31},\ \delta u_{32},\ \delta u_{33},\ \delta u_{41},\ \delta u_{42},\ \delta u_{43},$$

$$\delta\lambda_3)^T.$$

Applying boundary conditions for the two neighboring elements (2.43) and (2.44), the generalized internal forces cancel out. At free ends of the first and last elements, it is necessary to supply the boundary conditions. If N elements are used to describe a line in three dimensions, then the procedure results in 15+8(N-1) independent equations and coefficients. Then the global system of equations $\mathbf{A}\delta\mathbf{X}=\mathbf{B}$ are formed. Gauss elimination is used to solve the system of equations.

2.3.3.   Time Integration

The nonlinear differential dynamic equations are solved using Newmark-β method. At $t = 0$, or time step $K = 0$:

$$\gamma_{ikm} M_{njm}^{(0)} \ddot{u}_{kj}^{(0)} + \alpha_{ikm} B_m u_{kn}^{(0)} + \beta_{ikm} \tilde{\lambda}_m^{(0)} u_{kn}^{(0)} = \mu_{im} q_{mn}^{(0)} + f_{in}^{(0)} \qquad (2.50)$$

where $u^{(0)}$ and $\tilde{\lambda}^{(0)}$ are the solution of the static problem, and $\ddot{u}^{(0)}$ is the unknown. When dynamic analysis starts from a static initial equilibrium position and a ramp function is applied to the external forces, $\ddot{u}^{(0)} = 0$. The initial condition gives:

$$\dot{u}^{(0)} = 0 \tag{2.51}$$

at time step K (>0), $u^{(K)}$, $\dot{u}^{(K)}$, $\ddot{u}^{(K)}$ and $\tilde{\lambda}^{(K)}$ are predicted by:

$$\ddot{u}^{(K)} = \ddot{u}^{(K-1)}$$

$$u^{(K)} = u^{(K-1)} + \Delta t \dot{u}^{(K-1)} + \Delta t^2 (\frac{1}{2} - \beta)\ddot{u}^{(K-1)} + \Delta t^2 \beta \ddot{u}^{(K)}$$

$$\dot{u}^{(K)} = \dot{u}^{(K-1)} + \Delta t(1 - \gamma)\ddot{u}^{(K-1)} + \Delta t \gamma \ddot{u}^{(K)} \tag{2.52}$$

$$\tilde{\lambda}^{(K)} = \tilde{\lambda}^{(K-1)}$$

based on $u^{(K)}$, $\dot{u}^{(K)}$ and $\ddot{u}^{(K)}$, $\mathbf{M}^{(K)}$ and $\mathbf{q}^{(K)}$ can be computed.

Out of balance dynamic force for a small elongation element is hence:

$$R_{in}^{(K)} = f_{in}^{(K)} + \mu_{im}q_{mn}^{(K)} - \gamma_{ikm}M_{njm}\ddot{u}_{kj}^{(K)} - \alpha_{ikm}B_m u_{kn}^{(K)} - \beta_{ikm}\tilde{\lambda}_m^{(K)}u_{kn}^{(K)} \tag{2.53}$$

Corrections for displacement and $\tilde{\lambda}$ of a small elongation element can be obtained by solving the following equations (each element matrix is sequentially integrated into a global matrix):

$$\frac{\gamma_{ikm}}{\Delta t^2 \beta}M_{njm}^{(K)}\delta u_{kn}^{(K)} + (\alpha_{ikm}B_m + \beta_{ikm}\tilde{\lambda}_m^{(K)})\delta u_{kn}^{(K)} + \beta_{ikm}u_{kn}^{(K)}\delta\tilde{\lambda}_m^{(K)} = R_{in}^{(K)} \tag{2.54}$$

$$\beta_{ikm}u_{in}^{(K)}\delta u_{kn}^{(K)} - (\eta_{lm} + \tilde{\gamma}_{jlm}\varepsilon_j^{(K)})\left\{\frac{\delta\tilde{\lambda}^{(K)}}{EA} + (\rho_f A_f - \rho_i A_i)\frac{\delta y^{(K)}}{EA}\right\}\bigg|_l$$

$$= \frac{1}{2}(\tau_m + 2\eta_{lm}\varepsilon_l^{(K)} + \tilde{\gamma}_{jlm}\varepsilon_j^{(K)}\varepsilon_l^{(K)} - \beta_{ikm}u_{in}^{(K)}u_{kn}^{(K)}) \tag{2.55}$$

Finally, $u^{(K)}$, $\dot{u}^{(K)}$, $\ddot{u}^{(K)}$ and $\tilde{\lambda}^{(K)}$ are updated by:

$$u^{(K)} = u^{(K)} + \delta u^{(K)}$$

$$\dot{u}^{(K)} = \dot{u}^{(K)} + \frac{\gamma}{\beta \Delta t} \delta u^{(K)}$$

$$\ddot{u}^{(K)} = \ddot{u}^{(K)} + \frac{1}{\beta \Delta t^2} \delta u^{(K)}$$

$$\tilde{\lambda}^{(K)} = \tilde{\lambda}^{(K)} + \tilde{\delta}\lambda^{(K)}$$

$$(2.56)$$

The iteration of Equation (2.53) is terminated if $\delta u^{(K)}$ and $\delta\tilde{\lambda}^{(K)}$ are small enough. Then step $K+1$ of Equation (2.52) starts.

2.3.4. Bottom Support and Bottom Friction

The sea bottom is modeled by a spring system in the static simulation and a spring-damping system in the dynamic simulation of mooring lines.

The distributed force due to the spring (elastic sea bottom) is in vertical direction:

$$q^{Spring} = \begin{cases} \dfrac{S}{D}\left\{ D - (\mathbf{r} \cdot \mathbf{e}_y - D_{btm}) \right\} & D - (\mathbf{r} \cdot \mathbf{e}_y - D_{btm}) > 0 \\ 0 & D - (\mathbf{r} \cdot \mathbf{e}_y - D_{btm}) \leq 0 \end{cases} \qquad (2.57)$$

where D is the distance from the centerline of the rod to the most outer fiber of the rod (mooring line); D_{btm} is the coordinate of the ocean floor (in y-axis); and S is the submerged weight per unit lengths and described in Equation (2.58) for the case with

inside fluid and Equation (2.59) for the case without inside fluid:

$$S = \rho_t g A_t + \rho_i g A_i - \rho_f g A_f \tag{2.58}$$

$$S = \rho_t g A_t - \rho_f g A_f \tag{2.59}$$

Considering the ocean bottom support force, an extra term representing the distributed ocean bottom support force is added to the equation of motion. Multiplying both sides of the Equation (2.57) by the shape function $a(s)$ and then integrating it with respect to s from 0 to L of an element touching the bottom:

$$\int_0^L q^{Spring} a_i(s) ds = \mu_{im} \left\{ \frac{S}{D}(D + D_{btm}) \right\} \bigg|_m - \gamma_{ikm} \frac{S}{D} \bigg|_m u_{k2} \tag{2.60}$$

The distributed force due to damping is also in vertical direction:

$$q^{Damp} = \begin{cases} -C_c \dot{\mathbf{r}} \cdot \mathbf{e}_y & D - (\mathbf{r} \cdot \mathbf{e}_y - D_{btm}) > 0 \\ 0 & D - (\mathbf{r} \cdot \mathbf{e}_y - D_{btm}) \leq 0 \end{cases} \tag{2.61}$$

where C_c is the critical damping:

$$C_c = 2\sqrt{\frac{S}{D}\rho} \tag{2.62}$$

$$\int_0^L q^{Damp} a_i(s)ds = -\gamma_{ikm} C_c\big|_m \dot{u}_{k2} \tag{2.63}$$

Bottom friction is only considered in dynamic simulation of mooring lines. It could be modeled as:

$$q^{Frict} = \begin{cases} C_f fS \dfrac{\mathbf{r'}}{(1+\varepsilon)} & D-(\mathbf{r}\cdot\mathbf{e}_y - D_{btm}) > 0 \\ 0 & D-(\mathbf{r}\cdot\mathbf{e}_y - D_{btm}) \leq 0 \end{cases} \tag{2.64}$$

$$C_f = \begin{cases} -1 & v_t > C_v \\ -\dfrac{v_t}{C_v} & |v_t| \leq C_v \\ 1 & v_t < C_v \end{cases} \tag{2.65}$$

$$\int_0^L q^{Frict} a_i(s)ds = C_f f \left\{ S \dfrac{\mathbf{r'}}{(1+\varepsilon)} \right\}\bigg|_m \mu_{im} \tag{2.66}$$

where v_t is the tangential velocity, C_v the tolerance of tangential velocity and f the dynamic bottom friction coefficient.

Due to the presence of the ocean bottom, the shape coefficients γ and μ are no longer constants for the portion of the line around TDP and are integrated over the portion of an element that contacts with the sea bottom.

3. NON-DEGRADATION SOIL MODEL

3.1.   Model Description

A non-degradation P-y curve was proposed earlier for modeling the interaction

between the riser and the seabed which is based upon related laboratory tests and

numerical simulations (Dunlap et al., 1990; Willis and West., 2001; Giertsen et al., 2004;

Aubeny and Biscontin, 2008). This curve describes important phenomena occurring

during the interaction between SCR and the seabed, such as elastic rebound, riser-soil

separation, re-contact of soil and the riser and the plastic penetration. In a typical cycle

of large loading-unloading-reloading, the P-y curve may be divided into four different

paths (as shown in Figure 3.1). The first path describes the initial loading, where the P-y

relation follows along the backbone curve from Point 0 to 1. It depicts the initial

penetration of a riser into virgin soil. The penetration (y at Point 1) is determined by

equating W and P, where W is the vertical force applying on the seabed (usually the

submerged weight of the riser per unit length) and P is the soil resistance governed by

the backbone curve (Bridge et al., 2004). The initial penetration is usually much smaller

than that of the field observations made in the Gulf of Mexico. The observation indicated

that the maximum penetration of a riser is in the range of 4-5 riser diameters a few

months after the installation (Willis and West, 2001; Thethi and Moros, 2001). The

second and third path together describe the uplift (unloading) of the riser, corresponding

to the P-y curves from Point 1 to 2 and then from Point 2 to 3, respectively. When the

riser is being uplifted, the magnitude of the soil resistance to the riser reduces more quickly than the increase in the corresponding resistance during the initial penetration. After the resistance reaches zero, the soil may develop the suction (Dunlap et al., 1990; Bridge et al., 2004). The maximum suction (at Point 2), however, is significantly less than that of the corresponding maximum resistance (at Point 1). After Point 2, the suction of the soil diminishes and reaches zero at Point 3 when the riser completely separates from the soil. The fourth path describes the reloading of a riser. When the riser is being pushed again into the soil after the uplift, the riser will follow the curve from Point 3 to 1, which is much steeper than the path of initial loading (backbone curve). If the riser continues to experience the periodic loading cycle, the P-y relation will repeat the loop enclosed by the second, third and fourth path under the assumption of a non-degradation model. It should be noted that the loop area is greatly exaggerated in Figure 3.1 for the purpose of demonstrating.
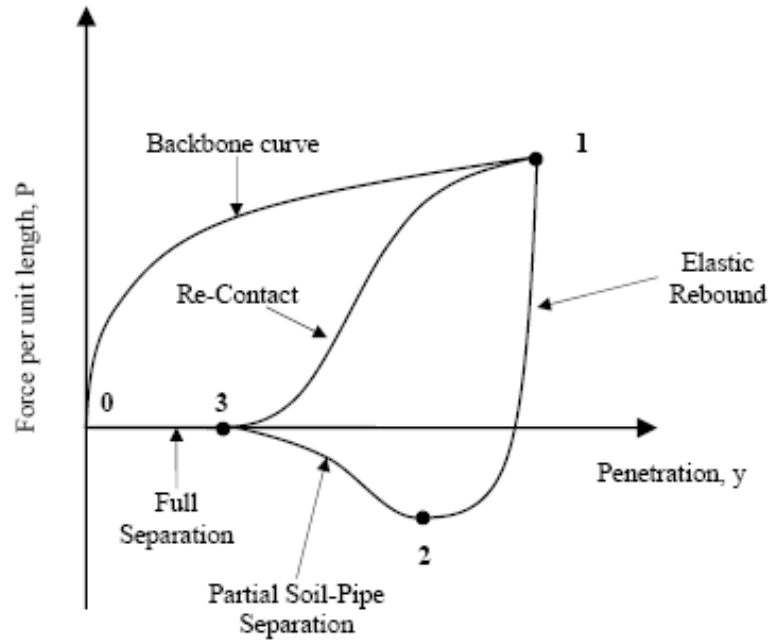
Figure 3.1. Typical P-y curve (extreme condition)

The empirical equations of backbone, elastic rebound, partial soil-pipe separation and re-contact paths of the curve were proposed by Aubeny and Biscontin (2008). They will be employed in this study. For the completeness, they are briefly described below. More detailed information about these empirical equations can be found in Jiao (2007), and Aubeny and Biscontin (2008, 2009).

The backbone curve is typically approximated by Equation (3.1),

$$P = N_p D \left(S_0 + S_g \, y \right) \tag{3.1}$$

where N_p is a dimensionless bearing factor, D the external diameter of the riser, S_0 the shear strength of soil at the seabed level, S_g shear strength gradient and P the soil

resistance to the riser per unit length.

The elastic rebound path (from Point 1 – 2) is described in Equations (3.2), (3.3), (3.4) and (3.5):

$$P = P_1 + \left(y - y_1\right) / \left(\frac{1}{k_0} - \frac{y - y_1}{(1+\omega)\,P_1} \right) \ , \qquad\qquad (3.2)$$

where k_0 is approximately related to soil undrained elastic modulus E_u through:

$$k_0 \approx 2.5\,E_u \qquad\qquad (3.3)$$

According to Aubeny's model (Jiao, 2007) $k_0 / S_0 = 660$.

$$y_2 = y_1 - \frac{(1+\omega)\,P_1}{k_0} \frac{1+\phi}{\omega - \phi} \ , \qquad\qquad (3.4)$$

$$P_2 = -\phi\,P_1 \ , \qquad\qquad (3.5)$$

where P_1 and y_1 are the resistance and penetration to seabed soil at Point 1, which are determined based on the backbone curve, and P_2 the maximum suction. ω and ϕ are dimensionless parameters and equal to 0.433 and 0.203, respectively (Jiao, 2007). The value of ϕ indicates that the maximum suction is about 20% of the maximum resistance.

The partial soil-pipe separation path (from Point 2 -3) is given by Equations (3.6) –

(3.8),

$$P = \frac{P_2}{2} + \frac{P_2}{4}\left[3\left(\frac{y - y_0}{y_m}\right) - \left(\frac{y - y_0}{y_m}\right)^3\right]$$ (3.6.a)

where

$$y_0 = \frac{y_2 + y_3}{2}$$ (3.6.b)

$$y_m = \frac{y_2 - y_3}{2}$$ (3.6.c)

$$y_3 = y_2 - \psi(y_1 - y_2)$$ (3.7)

$$P_3 = 0$$ (3.8)

where ψ is a dimensionless parameter and equal to 0.661.

Finally, the equations describing the re-contact path of the curve are given by,

$$P = \frac{P_1}{2} + \frac{P_1}{4}\left[3\left(\frac{y - y_0}{y_m}\right) - \left(\frac{y - y_0}{y_m}\right)^3\right]$$ (3.9.a)

where

$$y_0 = \frac{y_1 + y_3}{2} \tag{3.9.b}$$

$$y_m = \frac{y_1 - y_3}{2} \tag{3.9.c}$$

The curve in Figure 3.1 applies to the case that a riser experiences a periodic oscillation, that is, full contact and then full separation and the full contact again. If before the completion of a periodic oscillation the reversal motion of the riser takes place, the P-y curve will follow the dash line as depicted in Figure 3.2 The empirical formula for the dash curves was also described in Aubeny and Biscontin (2008),

$$P = P_r + \frac{y - y_r}{\dfrac{1}{k_0} + \chi \dfrac{y - y_r}{(1+\omega)P_1}} \tag{3.10}$$

where P_r and y_r are the force and penetration at a reversal point, and χ is a sign parameter ($\chi = 1$ for loading and $\chi = -1$ for unloading). It should be noted that this study assumes periodic oscillations of a riser and hence only the fully loading P-y curves are employed.
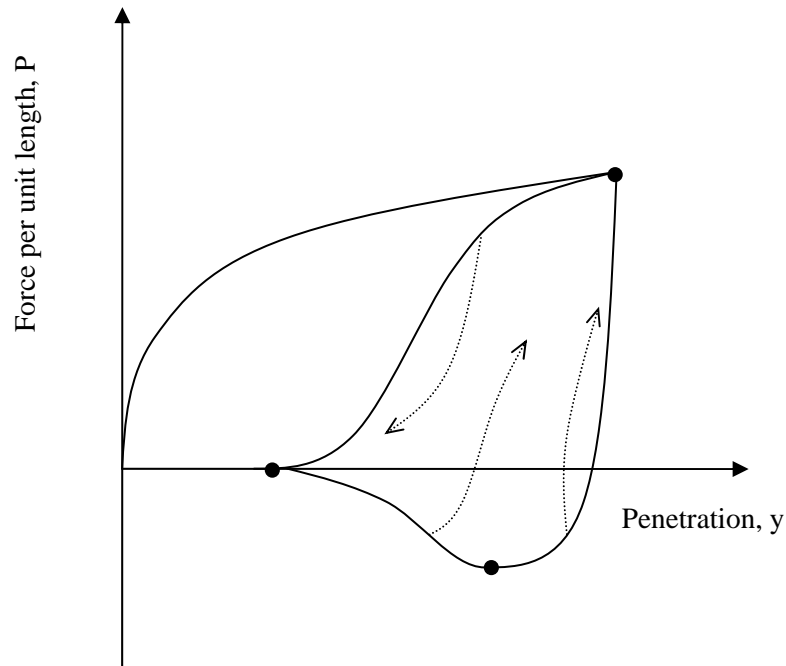
Figure 3.2. P-y curve (deflection reversals)

3.2. Extension of the Existing Version of CABLE3D Code

3.2.1. Soil Stiffness

In the original version of the CABLE3D, the resistance of seabed soil to a riser is modeled by a linear spring-dashpot system. The linear stiffness of the spring is chosen such that the penetration of a riser to the seabed is equal to R (the outside radius of the riser). This assumption does not take the effect of soil characteristics into account. Figure 3.1 shows that the soil stiffness is varying significantly in different stages of loading-unloading. Therefore incorporating a constant linear stiffness for soil into the model does not represent the true behavior of the soil. However, using the P-y curve, we

can have a better estimate of the equivalent soil stiffness. This will be an intermediate

stage between the original version of the CABLE3D and the more complicated extension

in which soil properties are derived from a P-y curve in every step.

Based on a non-degradation model assumption and regular motion of the upper-

end of the riser, the P-y curve does not vary significantly between consecutive cycles.

The equivalent stiffness of the soil is derived by calculating the slope of the line between

the point of initiation of elastic rebound and the point of maximum suction (points 1 and

2 in Figure 3.1.) Notice that the distance between the intersection of the elastic rebound

curve and point 3 in Figure 3.1 is exaggerated for better demonstration. Therefore,

choosing different points on the P-y curve does not result in drastic difference in the

estimation of the equivalent stiffness (Figure 3.3.)
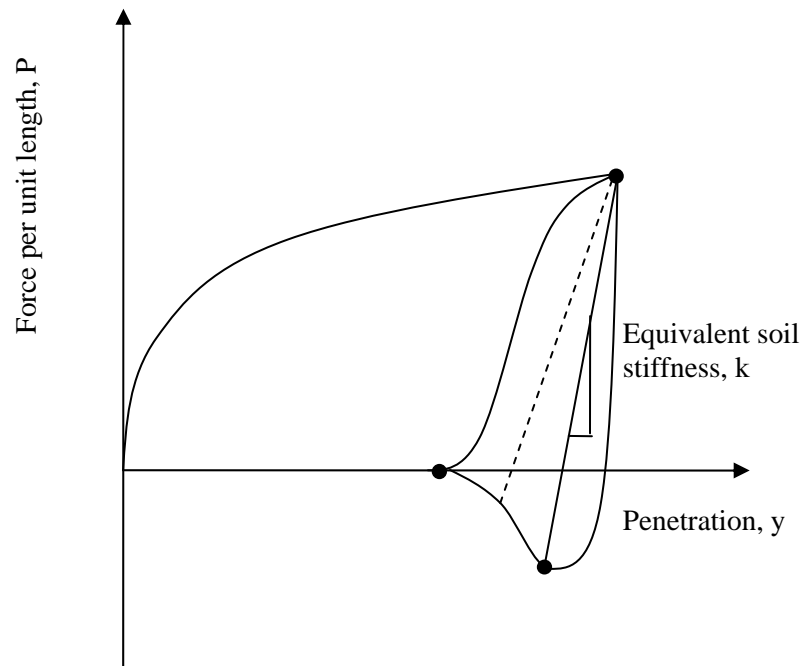
Figure 3.3. Equivalent soil stiffness

In the original version of CABLE3D it is assumed that the seabed has the stiffness of S/R, where S is the submerged weight of the riser and R is its external radius. Therefore the penetration of the riser under its own weight always would be equal to the radius of the riser. The supporting force is calculated from Equation (2.57).

In order to add the soil stiffness to the model, Equation (2.57) is modified as follows:

$$q^{Spring} = \begin{cases} k\left\{R - (\mathbf{r} \cdot \mathbf{e}_y - D_{btm})\right\} & R - (\mathbf{r} \cdot \mathbf{e}_y - D_{btm}) > 0 \\ 0 & R - (\mathbf{r} \cdot \mathbf{e}_y - D_{btm}) \leq 0 \end{cases} \qquad \textbf{(3.11)}$$

where k is the equivalent soil stiffness, R is the external radius of the riser, D_{btm} is the coordinate of the ocean floor (in y-axis), and $\mathbf{r} \cdot \mathbf{e}_y$ is the vertical coordinate of the centerline of the riser.

Since k is unknown at the beginning, the value of $y_0 = R - (\mathbf{r} \cdot \mathbf{e}_y - D_{btm})$ is estimated using the backbone curve (Equation 3.1) and assuming that supporting force (P) is equal to the submerged weight of the riser. The value of P is then modified by adding the vertical components of shear and tensile forces. As a result, a new value for y_1 will be acquired from Equation (3.1). Equation (3.11) is modified accordingly and iteration is continued until $|y_i - y_{i+1}| \leq \varepsilon$.

3.2.2. Damping Coefficient

Assuming a simple spring-dashpot model, the critical damping coefficient is equal

to:

$$C_c = 2\sqrt{k\,m}$$ (3.12)

where k is the stiffness and m is the mass.

In the original version of the CABLE3D, since the stiffness is equal to S/R, the critical damping coefficient is calculated using the following equation:

$$C_c = 2\sqrt{S\rho/R}$$ (3.13)

where S is the submerged weight of the riser per unit length, ρ the density of riser per unit length, and R is the radius of the riser . The damping ratio (the ratio of the damping coefficient to the critical damping coefficient) is also assumed to be always equal to 1. It should be noted that the above choice of damping coefficient does not allow for different properties of seabed soil. To allow for the support of the seabed described by the P-y curve and actual soil properties, the existing version of CABLE3D (Equation 2.62) is extended in this study, and Aubeny and Biscontin's model for relationship between soil penetration and supporting force are adopted.

Using the hysteresis loop (1-2-3-1 in Figure 3.1) the dissipated energy in one cycle could be calculated by integrating the supporting force with respect to vertical displacement, y. The equivalent viscous damping is then calculated by equating the dissipated energy from P-y curve to the equivalent elastic energy. A procedure similar to

what is recommended by DNV F105 is followed to obtain the equivalent damping ratio:

$$\zeta = \frac{1}{\pi} \frac{E_{\text{hystersis}}}{E_{\text{elastic}}}$$

(3.14)

where $E_{\text{hysteresis}}$ and E_{elastic} are depicted in Figure 3.4.
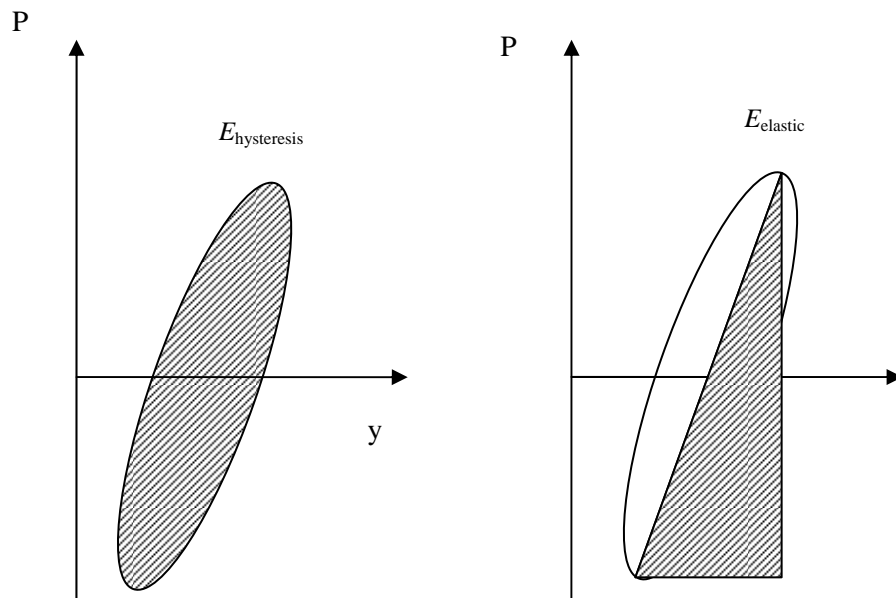
Figure 3.4. Equivalent soil damping

Knowing the area within the P-y curve and assuming the equivalent soil stiffness, the equivalent soil damping ratio is obtained.

3.3.   **Case Studies**

3.3.1.   Riser Characteristics

Two typical SCRs employed in the previous studies (Pesce et al., 2006; Xu et al., 2006) were selected for our numerical simulation. Their characteristics are summarized in Table 3.1. For simplification, it is assumed that the upper end of a riser is connected to a vessel through a hinge. It is noted that special joints, such as Flexjoints®, were employed as the connector between a riser and a vessel to reduce the bending moment of the riser near its upper end. Similar to a hinge joint, a Flexjoint allows a riser to rotate relatively with respect to the vessel. However, different from the former, the latter applies certain rotational stiffness at the upper end of a riser. Because the upper end connector is far away from the TDZ of a riser deployed in deep water, our simplification will not have significant effect on the bending moment of a riser near its TDZ.

Table 3.1. Properties of two risers

Property	unit	Riser 1	Riser 2
Length	m	5000	8000
Water Depth	m	1800	3000
Wall Thickness	mm	19.05	25.5
Internal Diameter	m	0.1651	0.355
External Diameter	m	0.2032	0.406
Axial Rigidity, EA	kN	$2.314*10^6$	$6.402*10^6$
Bending Stiffness, EI	kN.m2	9915	116360
Submerged Weight	kN/m	0.727	1.894
Mass	Kg/m	108	238.6
Top Tension	kN	1950	4750
Hang off angle (wrt vertical)	deg	20	22

3.3.2. Soil Properties

It is known that the shear strength of the soil increases linearly with depth. (Willis and West, 2001)

$$S = S_0 + S_g \, y \tag{3.15}$$

where S is the shear strength of the soil at the depth y measured from the surface of the seabed, and S_0 and S_g were defined in Equation (3.1). Table 3.2 presents the three sets of values for S_0 and S_g that represent three typical ranges of seabed soil (soft clay) in

the Gulf of Mexico. By default the median range of soil property will be used in the following numerical simulation, unless the other two ranges for soil are specially mentioned.

Table 3.2. Typical ranges of shear strength of seabed soil (soft clay) in the Gulf of Mexico (Willis and West, 2001)

Soil classification	S_0 (kPa)	S_g (kPa/m)
Lower range	1.2	0.8
Median range	2.6	1.25
Upper range	3.8	2.0

3.4. Approximation of a Non-degradation P-y Curve

In using CABLE3D to simulate the interaction between a riser and seabed soil, we assumed that the upper end of the riser was forced to have a regular heave or surge, presumably resulting from the oscillation of a floating surface structure, such as a semi-submersible, TLP and SPAR. It was found that to model the soil resistance to a riser exactly following a P-y curve is intensive in computation owing to the requirement of a small time step for the sake of numerical stability. Hence, first we explore if it is feasible to approximate the non-degradation P-y curve by a spring-dashpot model with an equivalent linear (or nonlinear) stiffness and damping coefficient (Nakhaee and Zhang,

2007). The equivalent linear/nonlinear stiffness is approximated by the center line of the

loop in the P-y curve, which connects Point 1 - 2. Hence, the equivalent stiffness allows

for the suction of the soil during the uplifting of a riser. The damping coefficient (in

terms of the ratio to the critical damping) is determined by matching the amount of

energy consumed by the spring-dashpot model to the energy loss represented by the area

of the loop in a P-y curve. Because the penetration of a riser varies along its TDZ even if

the heave or surge amplitude at the upper end remains constant, the area of the loop also

varies along the TDZ. Thus, given the motion amplitude at the upper end of a riser, the

damping coefficient was attempted by two different matching techniques. In using the

first one, the damping coefficient is obtained by matching with the area of the loop

where the greatest penetration of the riser into the seabed occurs. Because the loop area

is the greatest at the location of the greatest penetration, the damping coefficient derived

using the first technique is likely overestimated. The second technique is to match the

average area of P-y loops at three points evenly distributed along the TDZ (sketched in

Fig. 3.5). The damping coefficient derived using the second technique is in general

smaller than that obtained using the first technique.
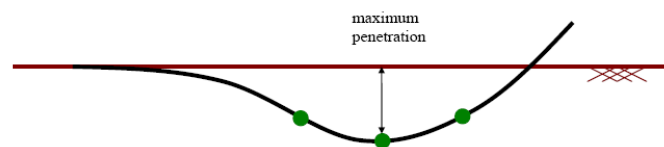
**Figure 3.5. Sketches for 1-point (at Node 1) and 3-point matching technique for
determining damping coefficient.**

To examine whether or not the simplified spring-dashpot model is able to approximate the related P-y curve, the dynamics of the two risers described in Table 3.1 was numerically simulated in the time domain when their upper ends are forced to have regular heave with 12 seconds period . To examine the different amplitudes of heave on the results of simulation, four heave amplitudes ranging from 0.5 – 5.0 m were considered in the simulation. Each simulation was made using three different extended versions of CABLE3D. The first allows for the support of seabed soil exactly following the non-degradation P-y curve, while the other two use the same equivalent stiffness but different damping coefficients derived respectively by one-point and three-point matching techniques described earlier. For an oscillating riser, the tension at its upper end, and the changes in its suspended length and bending moment at a reference point near the TDZ - where they reach maximum - are the important factors considered in the design. The related results of Riser 1 obtained using the three different extended versions of CABLE3D are summarized and compared in Tables 3.3 and 3.4.

Table 3.3. Results of Riser 1 obtained using three different extended versions of CABLE3D

	unit	Riser 1			
Heave amp.	m	0.5	1.0	2.0	5.0
Max Penetration	m	0.0407	0.0410	0.0418	0.0431
Equivalent damping ratio (using 1 point)	-	21.4	23.2	23.9	26.8
Equivalent damping ratio (using 3 points)	-	18.9	20.4	21.0	23.7
Moment variation at reference point (whole curve)	kN.m	+2.77 -2.71	+4.72 -4.95	+7.68 -7.33	+14.24 -13.92
Moment variation at reference point (1 point)	kN.m	+2.51 -2.42	+4.45 -4.70	+7.23 -6.92	+14.61 -14.11
Moment variation at reference point (3 points)	kN.m	+2.88 -2.86	+4.98 -4.87	+7.54 -7.29	+14.90 -14.62
Variation of suspended length (whole curve)	m	±1.88	±3.91	±8.12	±23.11
Variation of suspended length (1 point)	m	±1.81	±4.01	±8.69	±25.35
Variation of suspended length (3 points)	m	±1.86	±4.04	±8.24	±25.02
Variation of tension at upper end (whole curve)	kN	±10.4	±23.4	±40.7	±128.14
Variation of tension at upper end (1 point)	kN	±10.0	±24.2	±41.3	±139.0
Variation of tension at upper end (3 points)	kN	±10.4	±24.1	±40.9	±135.2

Table 3.4. Results of Riser 2 obtained using three different extended versions of CABLE3D

	unit	Riser 2			
Heave amp.	m	0.5	1.0	2.0	5.0
Max Penetration	m	0.192	0.199	0.207	0.218
Equivalent damping ratio (using 1 point)	-	24.2	26.3	30.3	38.8
Equivalent damping ratio (using 3 points)	-	19.8	22.5	25.7	32.1
Moment variation at reference (whole curve)	kN.m	+27.11 -26.61	+45.10 -44.83	+72.41 -72.02	+135.09 -133.98
Moment variation at reference (1 point)	kN.m	+27.82 -26.79	+45.34 -44.08	+73.12 -71.84	+137.13 -134.19
Moment variation at reference (3 points)	kN.m	+27.42 -26.80	+45.45 -45.01	+73.69 -72.24	+136.19 -134.11
Variation of suspended length (whole curve)	m	±3.84	±7.21	±13.33	±34.15
Variation of suspended length (1 point)	m	±3.72	±7.11	±13.09	±33.86
Variation of suspended length (3 points)	m	±3.94	±7.26	±13.64	±34.35
Variation of tension at upper end (whole curve)	kN	±33.3	±51.3	±89.7	±216.1
Variation of tension at upper end (1 point)	kN	±32.7	±51.1	±89.8	±216.6
Variation of tension at upper end (3 points)	kN	±33.4	±51.7	±91.0	±217.5

The maximum penetration into the seabed increases slightly with the increase in the heave amplitude at the upper end of the riser, which is expected. The maximum penetrations predicted using the three different versions of CABLE3D are virtually the

same and given in the third row of the table. In the fourth and fifth rows listed are the

equivalent damping coefficients, which were obtained using one-point (first) and three-

point (second) techniques, respectively. As expected, the values in the fourth row are

greater than the corresponding ones in the fifth. The table also shows that the equivalent

damping coefficient depends upon the maximum penetration. The larger the maximum

penetration is, the larger the corresponding equivalent damping coefficient. The

variation of bending moments reaches the maximum slightly above the TDZ. The

variations in the maximum bending moment obtained using three different versions are

given in the sixth to eighth rows. The comparison shows that the agreement is

satisfactory, especially between those in the sixth and eighth rows, indicating the three-

point match technique is better in determining the equivalent damping coefficient. The

variations in the suspended riser lengths are given in the ninth to eleventh rows and those

of the tension at the upper end of the riser in the twelfth to fourteenth rows. The

comparisons of predicted variations of suspended lengths and tensions show the similar

trend as in the case of predicted variation in bending moment. Therefore, in later

simulations the three-point matching technique will be used to determine the damping

coefficient of seabed soil.

Tables 3.5 and 3.6 demonstrate the effect of different soil types on the values of

stiffness and damping.

Table 3.5. Values of equivalent stiffness and damping ratio for different soil types (Riser 1, Heave amplitude 1m)

	unit	Lower range soil	Median range soil	Upper range soil
Equivalent damping ratio (using 3 points)	-	36.4	20.4	13.9
Equivalent stiffness	kN/m/m	98	137	222

Table 3.6. Values of equivalent stiffness and damping ratio for different soil types (Riser 2, Heave amplitude 1m)

	unit	Lower range soil	Median range soil	Upper range soil
Equivalent damping ratio (using 3 points)	-	41.0	22.5	15.1
Equivalent stiffness	kN/m/m	103	131	201

It should be notified that the value of equivalent stiffness for a certain soil type but different riser characteristics does not vary significantly. The change of equivalent stiffness for lower range of shear strength is 11.2%. This change for median range and upper range of soil shear strength is 9.3% and 7.9% respectively. However the values of equivalent damping ratio are significantly different for two risers. According to DNV-F105, the equivalent damping ratio is highly dependent on the characteristics of riser such as riser's diameter.

4. DEGRADATION SOIL MODEL

4.1.   Model Description

The non-degradation model described in the previous chapter neglects plastic deformation effects of cyclic loading on seabed soil. It states that a riser follows the same loop in a P-y curve repeatedly if cyclic loading remains the same.

In reality, cyclic loading degrades the soil condition. After many cycles of impact of the pipe on the soil, a plastic deformation occurs. This explains why the observed penetration of a riser into the seabed is much greater than computed penetration governed by the backbone curve or P-y curve. In addition, tri-axial shear tests show that the stiffness of cohesive soils is reduced with the increase in the number of loading cycles (Idriss et al., 1978). The degradation mechanism involves soil remolding in each downward and upward motion that may reduce the stiffness and strength of the soil (Fountaine et al., 2004). One explanation for the reduction is that when a pipe is pushed back toward soil after separation, the water underneath the pipe is pushed downward. The water is mixed with the soil and causes the erosion of the seabed (Clukey at al., 2005).

The degradation model (Aubeny and Biscontin, 2008) used in this study neglects the effects of water entrainment, reconsolidation, soil erosion and thixotropy on seabed soil. However, it considers the plastic deformation and consequently trenching development on the seabed.

The trench at the seabed smoothes the curvature of a riser near its TDZ, and thus reduces the maximum (spatial) change rate of bending moment near the TDZ and the variation of bending moment when the riser oscillates.

In order to estimate the trenching development on the seabed under cyclic loading, laboratory tests were conducted and an empirical formulation for the P-y curve considering the trench development in the seabed has been proposed by Aubeny and Biscontin (2008).

Figure 4.1 illustrates a P-y curve considering the soil degradation under multiple periodic loading cycles. Each individual P-y loop is similar to the corresponding non-degradation P-y loop except that the deformation of the soil. That is, y gradually increases after each loading cycle and consequently the loops translate to the right gradually.

It should be noted that the increase in deformation after each cycle plotted in the figure was greatly exaggerated for the purpose of demonstration. The plastic deformation of the seabed after one loading cycle is too minute to be discerned. However, the accumulation of the plastic deformation after many cycles is substantial and cannot be neglected. The estimate of the accumulation of the plastic deformation was empirically formulated and is briefly described below (Aubeny and Biscontin, 2008).
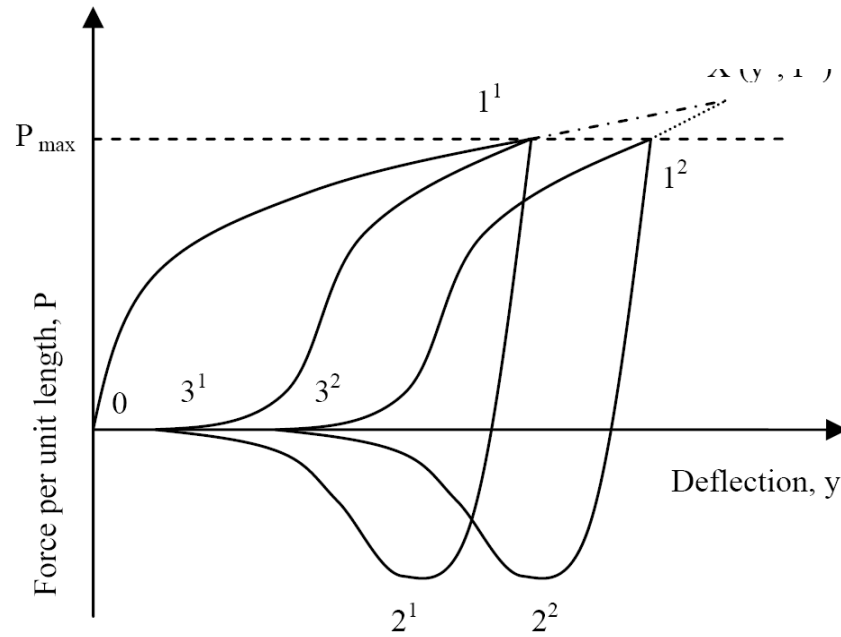
Figure 4.1. Sketch of a degradation P-y curve under multiple periodic loading cycles

The loop corresponding to one loading cycle can be defined by three points (1, 2, and 3) similar to a non-degradation P-y curve. The superscripts in the figure denote the different loading cycles but of the same magnitude of loading. After n^{th} cycle, instead of at Point 1^1, the end of reloading curve moves to a control Point X (y^n, P^n) due to the degradation of soil. The maximum penetration y^n in the nth cycle depends on an energy dissipation factor (λ_n) and initial penetration y_1^1.

$$y^n = y_1^1 + \alpha \lambda_n^{0.5} \tag{4.1}$$

where α is the degradation control factor (in this study, $\alpha = 0.003$), and λ_n is given by

the equation below:

$$\lambda_n = \sum_{i=1}^{n} \Delta y_i \qquad (4.2)$$

$$\Delta y_i = y_i^1 - y_i^3 \qquad (4.3)$$

Δy_i represents the maximum variation of penetration in the ith cycle. Considering that the loops in the P-y curve belonging to different cycles with the same loading pattern are almost identical except for a translation in y, the change in equivalent stiffness and damping coefficient are essentially negligible provided that the plastic deformation is subtracted from the current penetration.

For the degradation soil model, the elastic rebound path (from Point $1^i - 2^i$) is described in a hyperbolic form:

$$P = P_{max} + \left(y - y_1^i\right) / \left(\frac{1}{k_0} - \frac{y - y_1^i}{(1 + \omega) P_{max}}\right) \qquad (4.4)$$

where ω is a dimensionless parameter equal to 0.433 (Jiao, 2007).

The partial soil-pipe separation path (from Point 2^i -3^i) is given by Equations 4.5-4.8,

$$P = \frac{P_2^i + P_3^i}{2} + \frac{P_2^i - P_3^i}{4}\left[3\left(\frac{y - y_0}{y_m}\right) - \left(\frac{y - y_0}{y_m}\right)^3\right] \qquad (4.5.a)$$

$$y_0 = \frac{y_2^{\,i} + y_3^{\,i}}{2} \tag{4.5.b}$$

$$y_m = \frac{y_2^{\,i} - y_3^{\,i}}{2} \tag{4.5.c}$$

$$y_3^{\,i} = y_2^{\,i} - \psi(y_1^{\,i} - y_2^{\,i}) \tag{4.6}$$

$$P_2^{\,i} = -\varphi\, P_1^{\,i} \tag{4.7}$$

$$P_3^{\,i} = 0 \tag{4.8}$$

where ψ and ϕ are dimensionless parameters and equal to 0.661 and 0.203, respectively (Jiao, 2007).

Finally, the equations describing the re-contact path of the curve are given by,

$$P = \frac{P^n + P_3^{\,i}}{2} + \frac{P^n - P_3^{\,i}}{4}\left[3\left(\frac{y - y_0}{y_m}\right) - \left(\frac{y - y_0}{y_m}\right)^3 \right] \tag{4.9.a}$$

$$y_0 = \frac{y^n + y_3^{\,i}}{2} \tag{4.9.b}$$

$$y_m = \frac{y^n - y_3^{\,i}}{2} \tag{4.9.c}$$

Like the case of non-degradation model, if before the completion of a periodic oscillation the reversal motion of the riser takes place, the P-y curve will follow a curve as described by Aubeny and Biscontin (2008),

$$P = P_r + \cfrac{y - y_r}{\cfrac{1}{k_0} + \chi \cfrac{y - y_r}{(1 + \omega) P_1^{\,i}}}$$

(4.10)

where P_r and y_r are the force and penetration at a reversal point, k_0 is equal to $660 \times S_0$,

and χ is a sign parameter ($\chi = 1$ for loading and $\chi = -1$ for unloading).

4.2. Numerical Implementation

To allow for the development of a trench on the seabed, the existing version of

CABLE3D is extended (Nakhaee and Zhang, 2008). There are two major steps made in

the extension. First, an individual loop in the P-y curve corresponding to an individual

loading cycle is approximated by an equivalent linear or nonlinear stiffness and damping

coefficient, similar to the approximation made in a non-degradation P-y curve described

earlier.

Since the loops in a degradation P-y curve corresponding to different cycles but of

the same loading magnitude are similar except for a translation in y, the equivalent

stiffness and damping coefficient of all these loops are assumed to be time independent.

Secondly, the plastic deformation of the seabed beneath a riser at a later loading cycle

depends upon the number of loading cycles conducted before. That is, y* at the nth

loading cycle (see Fig. 4.1) is calculated as a function of number (*n*) based upon

Equations 4.1 – 4.3.

It is noted that the change in the plastic deformation is insignificant after just a few

loading cycles. Hence, for simplification only after hundreds of cycles the trench depth

along the TDZ is calculated. In this study, the trench depth beneath the riser is updated

every one hundred loading cycles. Then the bending moment, tension and bending

moment variation along the riser are calculated with respect to the updated (trenched)

seabed. To avoid the discontinuity in the shape of the trench, a smooth curve of normal

distribution shape is used for fitting the trench depth at different nodes of a riser along its

TDZ.

5. TRENCHING EFFECTS

5.1.   Case Studies

The two SCRs described in Table 3.1 are also employed in the simulation using the version of CABLE3D extended to allow for a degradation P-y curve. Considering that the dynamics of a riser varies significantly near its TDZ, we reduced the element size along a riser from 30 m in its suspended section to only 10 cm in the vicinity of its TDZ. However, in later description of simulation results, nominal nodes of uniform segment length (3.3 m for Riser 1 and 5m for Riser 2) will be adapted. It should be noted that the locations of the maximum bending moment, maximum variation of the bending moment, the deepest trench depth near the TDZ, can be actually pinpointed with an error less than 10 cm because the distance between two nodes near the TDZ is actually 10 cm in the simulation.

Figures 5.1 and 5.2 respectively show the gradual increase in the trench depth under Riser 1 and 2 with the increase in time (or the number of loading cycles). In both cases, the cyclic loading applied on the seabed results from a forced periodic heave of amplitude 1 m and period 12 s at the upper end of the risers. It is observed that initially the rate of trenching is relatively fast but slows after many cycles. This is expected because the trenching development is related to the square root of λ_n as shown in Equation 4.1. Although the rate of trenching slowed from 180-hour (54,000 cycles) to 300-hour (90,000 cycles), the trenching development still remains noticeable. It is also

noticed that at the beginning the trench is almost symmetric with respect to the center of the TDZ (located at 80 cm left from Node 17 in Figure 5.1 and 40 cm left from Node 57 in Figure 5.2). After 100 hours of cyclical loading, the deepest point of the trench (located right at Node 17 in Figure 4.2 and 10 cm right from Node 57 in Figure 5.2) moves slightly towards the left end of the TDZ (close to the suspended portion of a riser). The trench depth in the case of Riser 2 is greater than that in the case of Riser 1. It is expected because the submerged weight per unit length of Riser 2 is heavier than that of Riser 1. The simulation also confirms our assumption that the trenching between two consecutive loading cycles is extremely small (less than 0.002 mm per loading cycle in the case of Riser 1 and less than 0.005 mm in the case of Riser 2, when heave amplitude is 1m and period 12s). However, after several hundreds of cycles the trench development on the seabed is noticeable as shown in both figures. To verify whether or not it is sufficient to up-date of trench depth for every 100 loading cycles, the corresponding numerical simulation has been conducted based upon the up-date of trench depth for every 50 cycles. It is found that the related numerical results are virtually the same. Therefore, it is justified to up-date the trench depth (or plastic deformation) at the seabed for every 100 loading cycles.
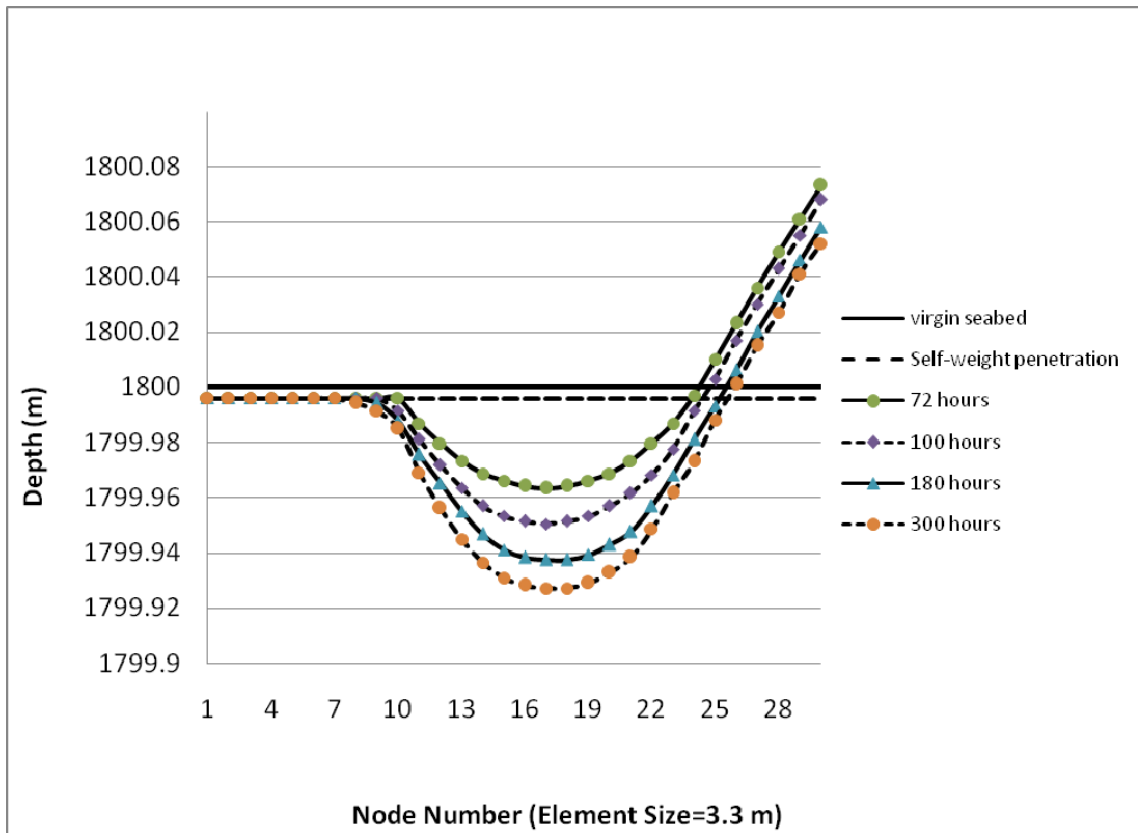
Figure 5.1. Trench development under Riser 1 (heave amplitude = 1m, period = 12s, median range of shear strength)
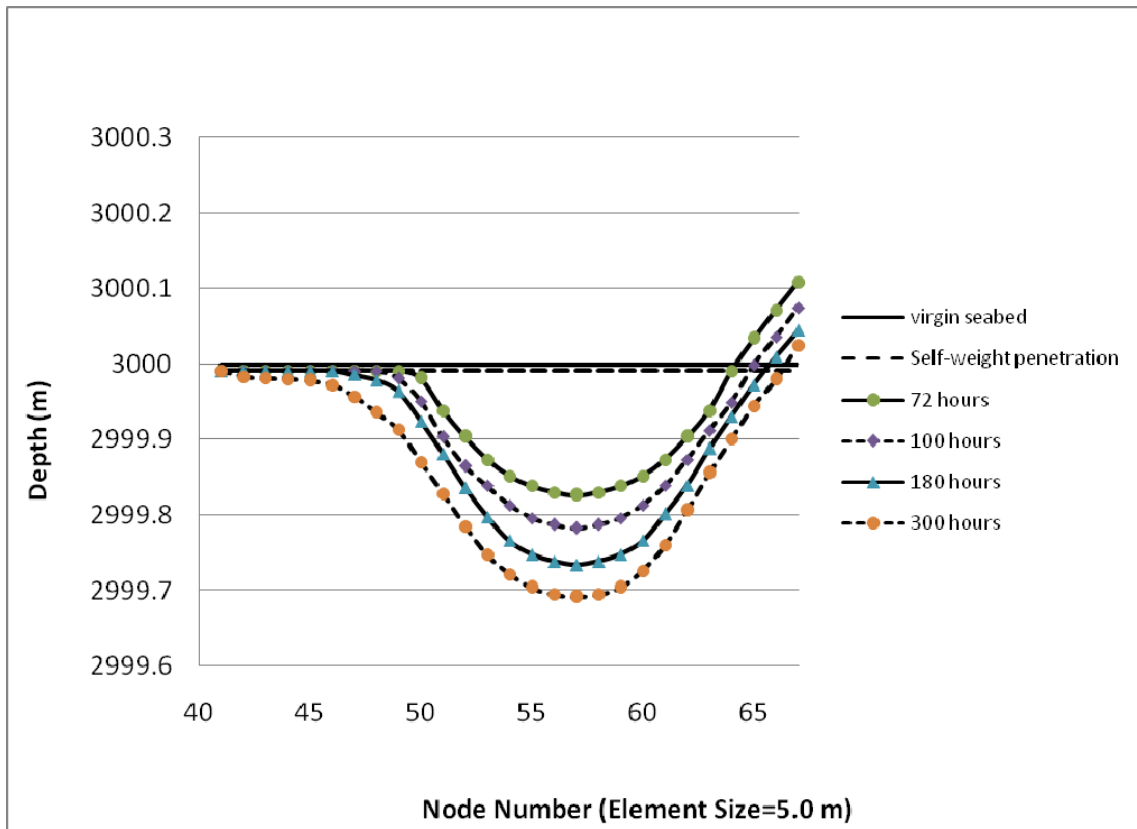
Figure 5.2. Trench development under Riser 2 (heave amplitude = 1 m, period = 12 s, median range of shear strength)

Figures 5.3 and 5.4 respectively depict the maximum variation of bending moment near the TDZ of Riser 1 and 2 as a function of time after they experience forced heave. Both figures show that the maximum variation of bending moment near the TDZ gradually reduces due to the development of trenching. It should be noted that the maximum variation in bending moment in the TDZ shown in Figures 5.3 and 5.4 does not always occur at the same location during the development of trenching. As demonstrated in Figure 5.5, at different nodes the variation of the bending moment

decreases or even increases with the development of trenching. Hence, the maximum variation of bending moment near the TDZ likely occurs at the different nodes during the trenching development. In the case of Riser 1, after 140-hour cycle loading the location of the maximum variation of bending moment shifted from Node 34 to Node 33. Figure 5.5 shows the variation of bending moment at Node 34 reduces from 5.68 kN.m to 5.05 kN.m. At Node 33, however, the variation increases from 4.52 kN.m to 5.2 kN.m. Thus, at this moment Node 33 becomes the location of the maximum variation of bending moment near the TDZ. It should be noted that although the variation of bending moment at Node 33 has increased and becomes the maximum near the TDZ it is still smaller than the initial maximum variation of bending moment (5.68 kN.m at Node 34). The shift in the location of the maximum variation of bending moment is related to the deepening and increasing the length of the trench.
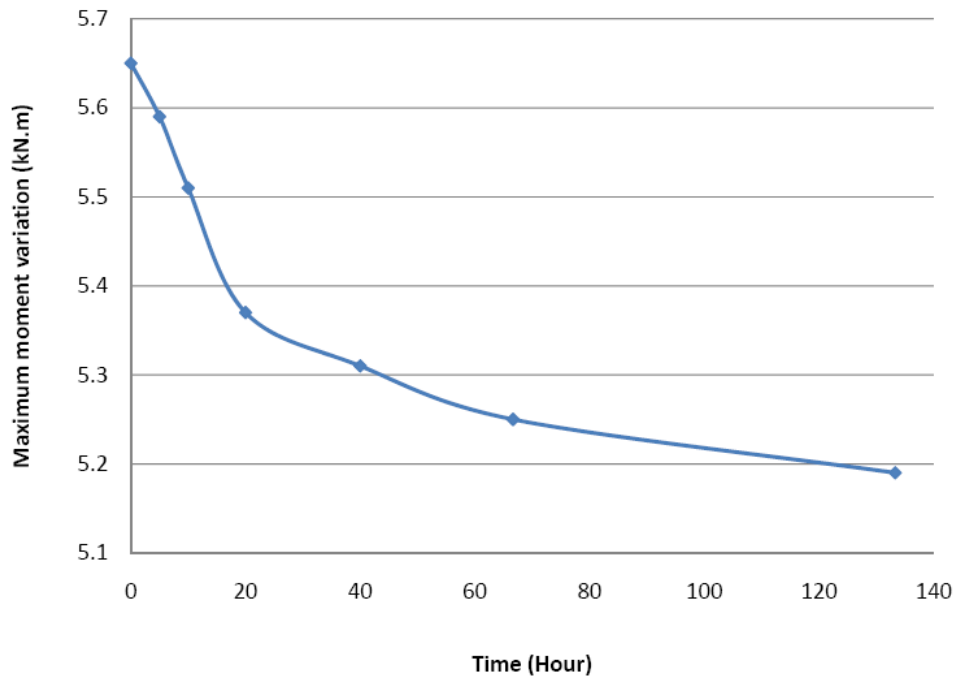
Figure 5.3. Maximum moment variation along Riser 1 near TDZ (heave amplitude = 1 m, period = 12 s, median range of shear strength)
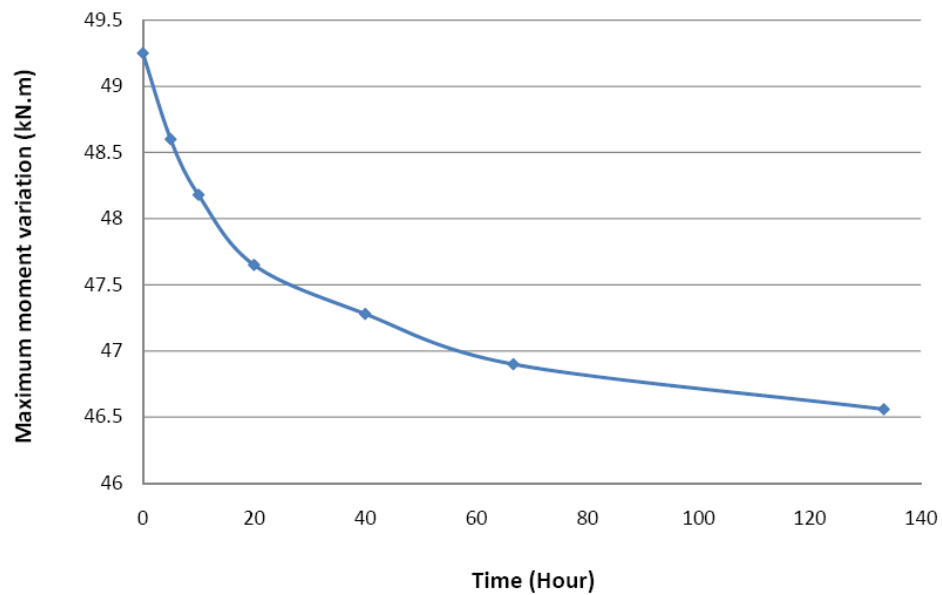

Figure 5.4. Maximum moment variation along Riser 2 near TDZ (heave amplitude = 1 m, period = 12 s, median range of shear strength)
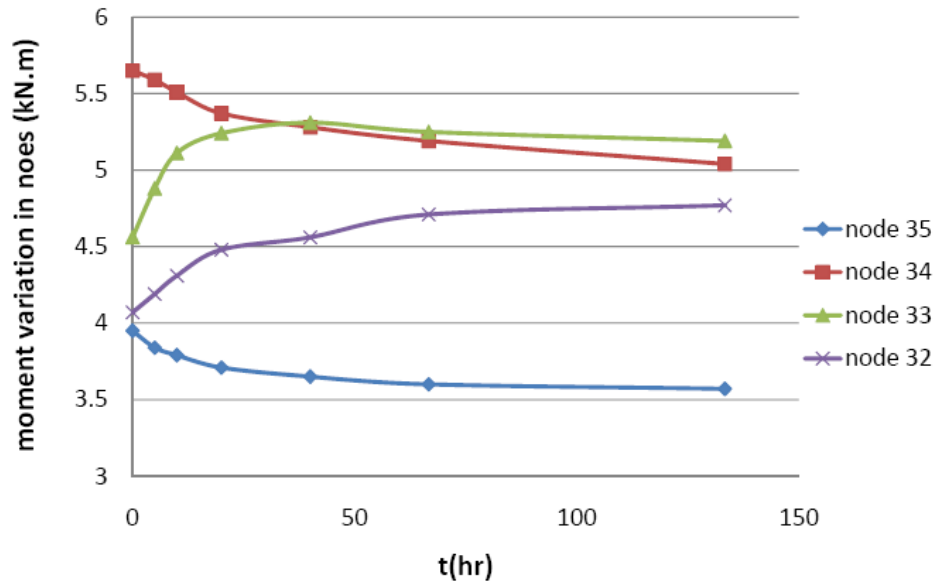
Figure 5.5. Moment variation in different nodes along Riser 1 (heave amplitude = 1 m, period = 12 s, median range of shear strength)

To explore the effect of different soil shear strengths on the maximum variation of bending moment, we also conducted numerical simulation on Riser 2 interacting respectively with the soils of three different ranges of stiffness, namely, lower range, median range and upper range as quantified in Table 3.3. For the same forced heave of amplitude (0.5m) and period (12s) at the upper end of Riser 2, the deepest trench is developed on the seabed of soils of lower range stiffness. As expected, the deepest trench results in largest reduction in the maximum variation of bending moment.

Figure 5.6 shows that after 480-hour heave induced cyclical loading the reduction in the maximum variation of bending moment of Riser 2 may reach 35%, 20% and 14% with respect to their corresponding initial values when interacting respectively with the

soils of lower, median and upper range stiffness. In interacting with the soil of the same (median) range of stiffness, the rate of the reduction in the maximum variation of bending moment of a riser depends on the amplitude of forced heave at its upper end. Figure 5.7 shows the reduction in the maximum variation of bending moment near the TDZ of Riser 2 normalized by the corresponding initial value (at the beginning of trench development) decreases with the increase in heave amplitude. The same trend is also observed in the case of Riser 1 experiencing forced heave and surge as shown in the figure on P. 68. Hence, the rate of the reduction in the maximum variation of bending moment is more substantial for a riser under sea states more frequently occurring in nature (which likely result in small heave or surge amplitude at the upper end of a riser).
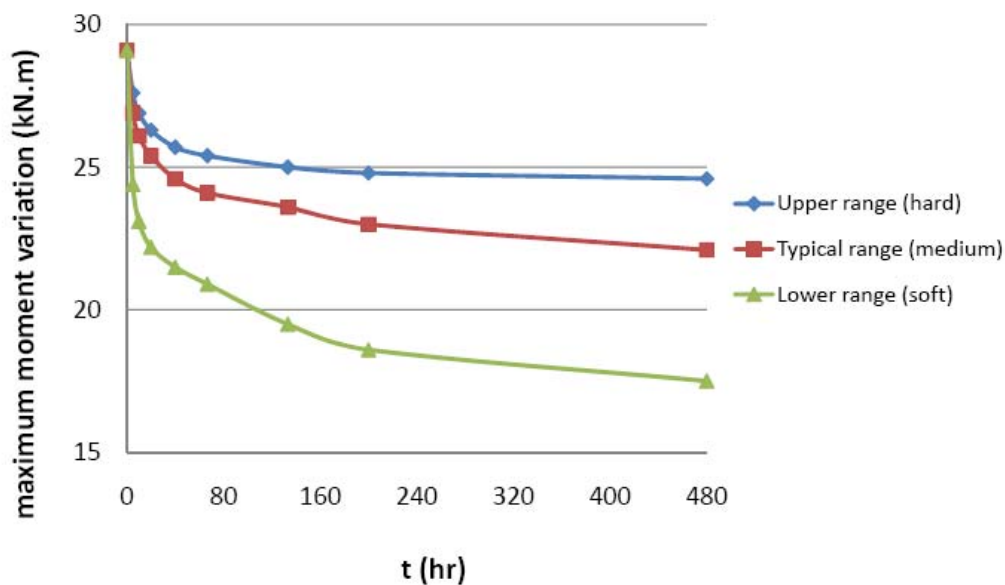

Figure 5.6. Maximum moment variation in Riser 2 for different shear strengths of soil (heave amplitude = 0.5 m, period = 12 s)
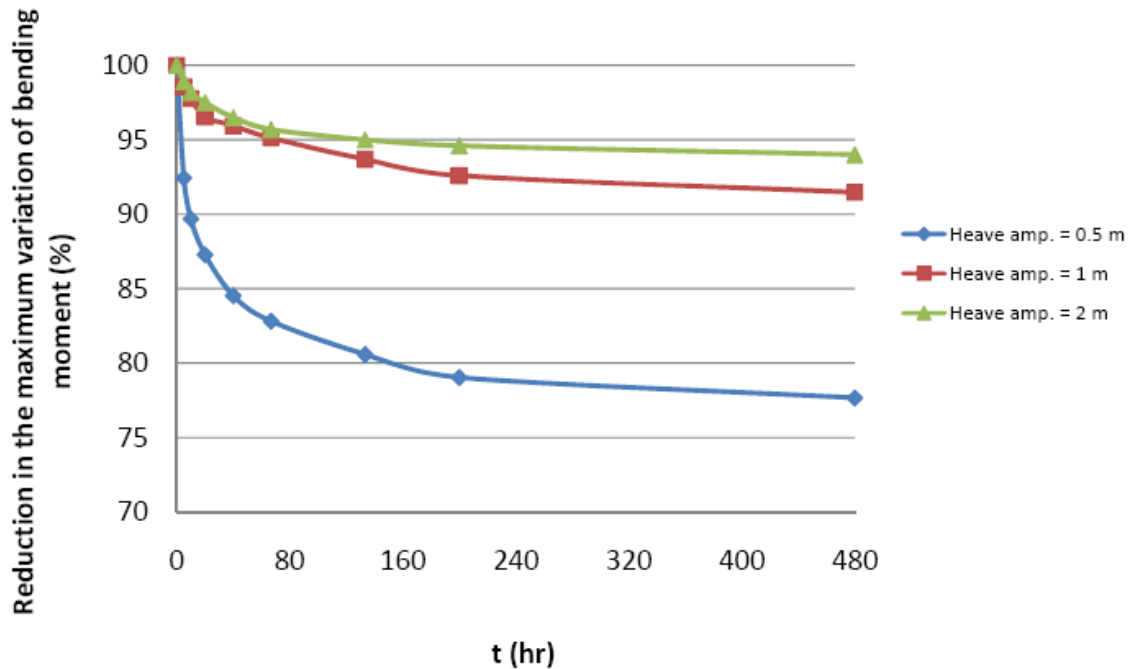
Figure 5.7. Reduction in the maximum variation of bending moment normalized by the related initial values (Riser 2, Heave period = 12 s, Median range of shear strength)

The corresponding numerical simulations were also made for Riser 1 experiencing forced surge at its upper end to examine whether or not the trends of the trench development and reduction in maximum variation of bending moment are qualitatively similar to those induce by forced heave. A SCR connected to a SPAR likely experiences relatively large surge at its upper end, which results mainly from the slow-drift motion of a SPAR near its surge resonance period. Hence, the forced periodic surge at the upper end of Riser 1 was chosen to have the amplitudes of 5, 10 and 20 m and period of 100 s. Figure 5.8 depicts the maximum trench depth developed on the seabed as a function of time in the case of Riser 1 experiencing periodic surge at its upper end. The trench depth increases with the increase in time and the rate of increase gradually slows. This trend is

similar to that observed in the cases of Riser1 and 2 experiencing forced heaves.

5.2. Surge Motion

Figure 5.9 shows that the reduction in the maximum variation of the bending moment near the TDZ as a function of time for Riser 1 experiencing the periodic forced surges. The trend observed in this figure is similar to those observed in Figure 5.7. For comparison, also plotted are the related values of Riser 1 experiencing forced heave at its upper end. Because the periods of forced surge (100s) and heave (12s) are quite different, the horizontal coordinate in this figure denotes the number of loading cycles instead of time. It is observed that the trend of reduction in the maximum variation of bending moment as a function of loading cycles is similar. However, to reach similar magnitude in the reduction, the amplitude of forced surge is roughly 10 times as that of forced heave. This is because that forced surge induces a much smaller variation in suspended length of a riser than that induced by forced heave of the same amplitude, especially when a riser is deployed in relatively deep water. This phenomenon was observed earlier by Theckumpurath and Zhang (2006) in the case of two SCRs connected to a truss SPAR. In addition, because the surge period is much greater than the heave period it takes much longer time for a riser experiencing forced surge to have the similar reduction in the maximum variation of bending moment than in the case of forced heave motion.
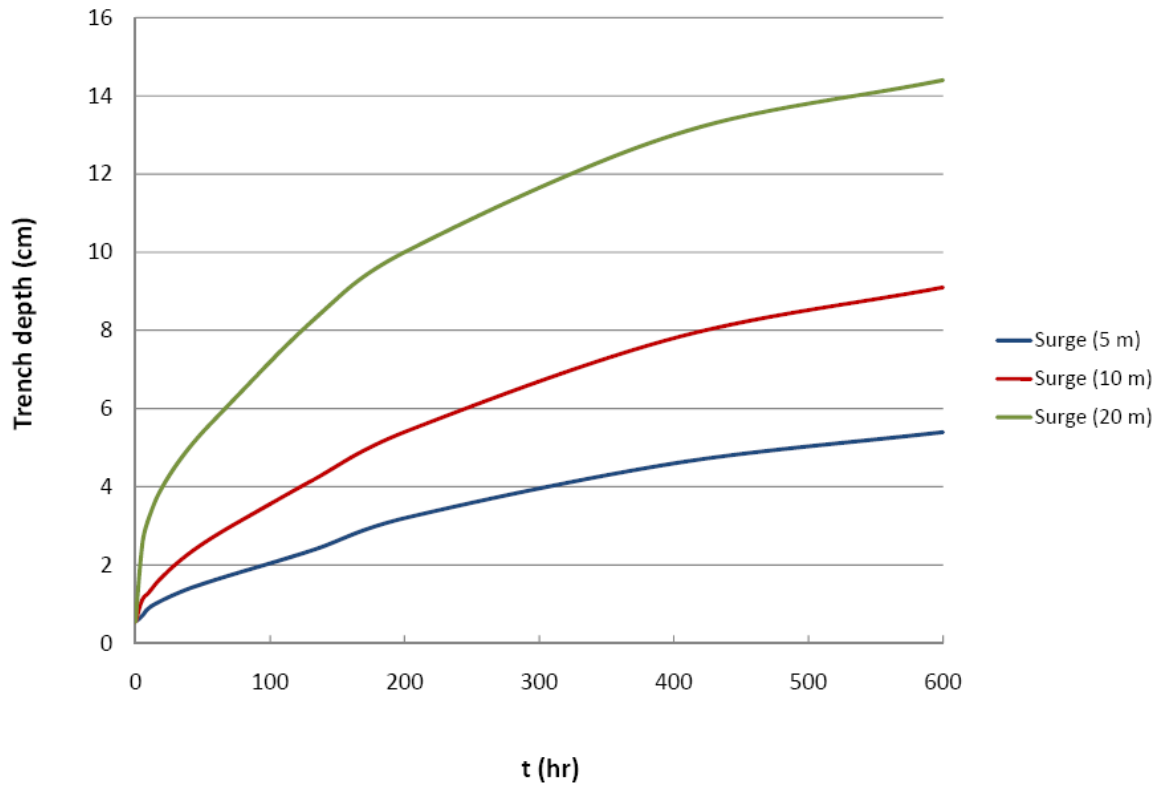
Figure 5.8. The maximum trench depth of Riser 1 in its TDZ at the seabed of median range shear strength (surge period = 100 s and related surge amplitudes are 5, 10, and 20 m, respectively)
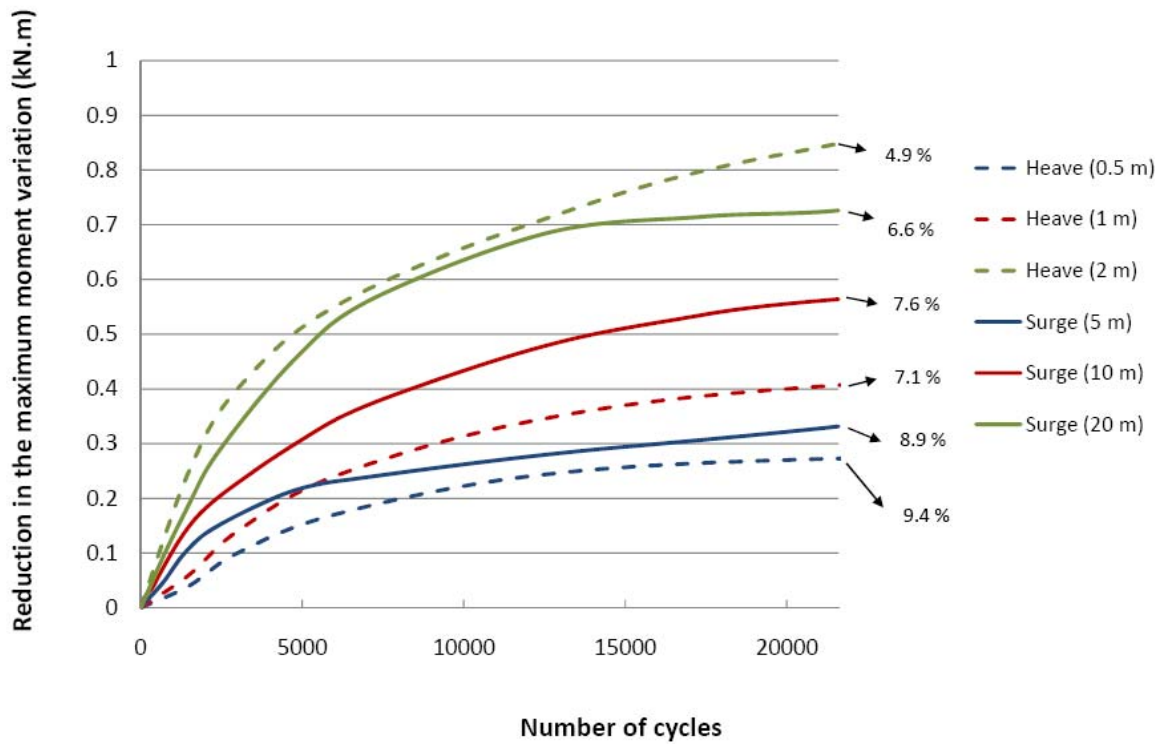
Figure 5.9. Reduction of the maximum bending moment variation of Riser 1 near its TDZ (surge period = 100 s and heave period = 12 s; Percentages on the graph show the ratio of the reduction of the bending moment with respect to the initial value)

6. RESULTS AND CONCLUSION

6.1. Discussion of the Results

The total stress along a riser results from both bending moment and tension. In the cases of Riser 1 and 2, the variation of the tension induced by forced surge or heave is found to be about 1 - 3% of the mean tension and less than 10% of that induced by the maximum variation of bending moment near the TDZ. Therefore, the stress level (or stress fluctuation) is dictated by the variation in the bending moment. The variation of bending moment is related to the stress level through the following equation:

$$\Delta\sigma = \frac{R}{I}\Delta M \tag{6.1}$$

where $\Delta\sigma$ is the stress level, ΔM, the variation of bending moment , R the radius, and I the moment of inertia of the cross section area of a riser. Assuming that the radius and moment of inertia of a riser remain constant near its TDZ, the stress level is proportional to the variation of bending moment. Following the X' S-N curve proposed by API RP 2A given below,

$$N = 2.5\times10^{13}\left(SCF\times\Delta\sigma\right)^{-3.74} \tag{6.2}$$

where N is the number of allowable loading cycles at a certain stress level and SCF the

stress concentration factor, the number of allowable loading cycles can be estimated. Assuming that SCF remains unchanged during the trenching development, the ratio of allowable loading cycles with the trenching to those without the trenching is hence related to the ratio of the variation of bending moment during the trenching development to that without trenching through Equation (6.3).

$$\frac{N_{\text{trenching}}}{N_{\text{no-trenching}}} = \frac{1}{T_{\text{total}}} \int_0^{T_{\text{total}}} \left(\frac{\Delta M(t)}{\Delta M_{\text{no-trenching}}} \right)^{-3.74} dt \tag{6.3}$$

where T_{total} is the total duration for the trenching development, $\Delta M(t)$ is the maximum variation of bending moment at time t, and $\Delta M_{\text{no-trenching}}$ is the maximum variation of bending moment in the absence of the trenching development.

As shown in Figure 5.3, the maximum variation of the bending moment near the TDZ of Riser 1 is 5.70 kN.m before the trenching development. After 140 hours of forced heave of amplitude 1m and period 12s, the maximum variation of bending moment gradually reduces to 5.20 kN.m. Similarly, the maximum variation of the bending moment near the TDZ of Riser 2 before the trenching development is 49.20 kN.m (Figure 5.4).

After 140 hours of forced heave of amplitude 1m and period 12s, it gradually reduces to 46.50 kN.m. For computing the ratio of allowable loading cycle, Equation 6.3 is numerically integrated using a Trapezoidal rule, where T_{total} is equal to 140 hour and the increment time used in the numerical integration is $\Delta T = 5$ hours. The computation given in Table 6.1 shows that the increase in the number of allowable loading cycles for Riser 1 and 2 is about 30% and 18%, respectively.

It is noted that maximum variation of bending moment decrease more in ratio to the initial maximum variation when the amplitude of heave or surge is small and/or seabed soil is of small shear strength. The increase in allowable cycles can be significantly higher than 30%. For example, 20% reduction in the maximum variation of bending moment (that has occurred in Figure 5.7 for Riser 2) may increase the allowable cycles by 100%.

Table 6.1. Numerical integration of the ratio of allowable loading cycles during 140-hr trenching development over median strength soil (Heave amp= 1m, T=12 s)

t (hr)	Riser 1		Riser 2	
	Maximum Moment Variation (kN)	$\left(\Delta M(t) \middle/ \Delta M_{\text{no-trenching}}\right)^{-3.74}$	Maximum Moment Variation (kN)	$\left(\Delta M(t) \middle/ \Delta M_{\text{no-trenching}}\right)^{-3.74}$
0	5.65	1	49.20	1.00
5	5.62	1.02	49.14	1.00
10	5.51	1.10	48.50	1.06
15	5.46	1.13	48.27	1.07
20	5.43	1.16	48.08	1.09
25	5.41	1.18	47.97	1.10
30	5.39	1.19	47.86	1.11
35	5.37	1.21	47.76	1.12
40	5.35	1.22	47.67	1.13
45	5.34	1.24	47.60	1.13
50	5.33	1.25	47.55	1.14
55	5.32	1.25	47.49	1.14
60	5.31	1.26	47.44	1.15
65	5.31	1.26	47.41	1.15
70	5.30	1.27	47.36	1.15
75	5.29	1.28	47.32	1.16
80	5.28	1.29	47.28	1.16
85	5.27	1.30	47.25	1.16
90	5.27	1.30	47.21	1.17
95	5.26	1.30	47.16	1.17
100	5.26	1.31	47.14	1.17
105	5.25	1.31	47.10	1.18
110	5.25	1.32	47.09	1.18
115	5.24	1.32	47.08	1.18
120	5.24	1.33	47.05	1.18
125	5.23	1.33	47.02	1.18
130	5.23	1.33	47.00	1.19
135	5.23	1.33	46.99	1.19
140	5.23	1.34	46.99	1.19
Trapezoidal rule		**1.25**		**1.14**

Table 6.2. Numerical integration of the ratio of allowable loading cycles during 140-hr trenching development over lower range strength soil (Heave amp= 1m, T=12 s)

	Riser 1		Riser 2	
t (hr)	Maximum Moment Variation (kN)	$\left(\Delta M(t)\big/\Delta M_{\text{no-trenching}}\right)^{-3.74}$	Maximum Moment Variation (kN)	$\left(\Delta M(t)\big/\Delta M_{\text{no-trenching}}\right)^{-3.74}$
0	5.65	1.00	49.20	1.00
5	5.21	1.35	46.88	1.20
10	5.08	1.49	45.66	1.32
15	4.99	1.59	44.76	1.42
20	4.92	1.68	44.43	1.46
25	4.88	1.74	44.28	1.48
30	4.86	1.75	44.05	1.51
35	4.85	1.77	43.88	1.53
40	4.83	1.80	43.79	1.55
45	4.82	1.81	43.74	1.55
50	4.82	1.82	43.71	1.56
55	4.81	1.83	43.66	1.56
60	4.80	1.83	43.62	1.57
65	4.80	1.84	43.59	1.57
70	4.79	1.86	43.53	1.58
75	4.78	1.87	43.51	1.58
80	4.77	1.88	43.47	1.59
85	4.77	1.89	43.46	1.59
90	4.76	1.89	43.40	1.60
95	4.76	1.90	43.35	1.60
100	4.75	1.91	43.35	1.61
105	4.75	1.91	43.31	1.61
110	4.75	1.92	43.32	1.61
115	4.74	1.93	43.31	1.61
120	4.73	1.94	43.27	1.62
125	4.73	1.94	43.24	1.62
130	4.73	1.94	43.23	1.62
135	4.73	1.94	43.22	1.62
140	4.73	1.95	43.22	1.62
Trapezoidal rule		**1.80**		**1.54**

6.2.   Effect of Wave Period on Trenching

A riser will experience the loads and motions of different sea environments during its service life. It would be useful if a relationship between the wave period and trenching could be obtained. In order for this, several comparisons are made.

Maximum trenching under Riser 1 and Riser 2 is calculated for constant wave type, wave height and different wave periods. Tables 6.3-6.6 summarize these results.

Table 6.3. Maximum trenching after 300-hr over median strength soil (Riser 1, Heave height= 1m)

Motion period (s)	Trench depth (m)
6	0.093
12	0.078
18	0.066
24	0.057
30	0.050

Table 6.4. Maximum trenching after 300-hr over median strength soil (Riser 1, Heave height= 5m)

Motion period (s)	Trench depth (m)
6	0.241
12	0.218
18	0.146
24	0.117
30	0.096

Table 6.5. Maximum trenching after 300-hr over median strength soil (Riser 2, Heave height= 1m)

Motion period (s)	Trench depth (m)
6	0.413
12	0.331
18	0.264
24	0.228
30	0.199

Table 6.6. Maximum trenching after 300-hr over median strength soil (Riser 2, Heave height= 5m)

Motion period (s)	Trench depth (m)
6	1.018
12	0.843
18	0.779
24	0.568
30	0.421

As it could be observed in all these tables, reducing the wave period, while the wave height is constant, will result in increasing the trench depth. This is of no surprise since all these results are compared at 300-hour time pass. Therefore, waves with the lower period will have more occurrences during this period. If we look back at equations 4.1 and 4.2 we will notice that the number of wave occurrence directly affects energy

dissipation factor (λ_n) which in return changes maximum penetration.

To observe the effect of wave period on the trenching at similar occurrences, another comparison is made. These results are summarized in Tables 6.7-6.9.

Table 6.7. Maximum trenching after 90,000 occurrences over median strength soil (Riser 1, Heave height= 1m)

Motion period (s)	Trench depth (m)
6	0.081
12	0.078
18	0.076
24	0.074
30	0.073

Table 6.8. Maximum trenching after 90,000 occurrences over median strength soil (Riser 2, Heave height= 1m)

Motion period (s)	Trench depth (m)
6	0.341
12	0.331
18	0.324
24	0.320
30	0.317

As you it could be seen in these tables, the lower the period, the maximum the

trenching will be at the same number of occurrences. There is a 9.9% and 7.0% of reduction in the trenching in Riser 1 and 2 respectively as the period changes from 6s to 30 s. This could be described as follows. A motion with lower period and same wave height results in higher velocities and acceleration in the upper end and as a result the dynamic forces and moments will increase. The downward force at the seabed level is a summation of static (riser weight) and dynamic forces. Since the dynamic variation of tension is higher for the lower periods, the maximum trenching will be higher too.

Another comparison is made for different wave periods and different wave heights. It is assumed that the same motion magnitude occurs in heave and surge for different wave periods.

Table 6.9. Maximum trenching after 90,000 occurrences over median strength soil (Riser 1)

Motion	Trench depth (m)
Heave = 5m, period = 12 s	0.218
Surge = 5m, period = 60 s	0.039

As it could be seen, the trench depth is almost 7 times bigger for a have motion of the same magnitude of surge motion. One obvious explanation is that the wave period for heave motion is less than of surge motion. But as compared with the results of Table 6.6, we notice that ratio of trench depth in two cases are much higher here. This could be explained as follows: According to Theckumpurath and Zhang (2006), ratio of change in suspended length to motion is different for Heave and surge motion. For the case

study mentioned in their paper, this ratio is 19.89 for heave motion and only 0.714 for surge motion. It means that for a similar motion magnitude, heave will cause more than 27 times change in the suspended length comparing to a surge motion. Also according to Pesce et al. (2006) the excursion of the TDP is the main reason for the variation of tension and bending moment in the TDZ. Therefore it could be anticipated that a heave motion will cause a significantly deeper trench comparing to a surge motion of the same magnitude.

6.3.   Conclusion

A numerical scheme for analyzing the dynamics of risers, CABLE3D, has been extended to allow for two different soil models: first non-degradation and then degradation. The non-degradation model does not consider the effects of plastic deformation of seabed soil on the dynamics of a riser near the TDZ. It, however, provides a more accurate stiffness and damping coefficients of the soil comparing to traditional elastic seabed simulation. These coefficients are then used in a degradation model that accounts for the plastic deformation and consequently trenching development at the seabed based on a degradation P-y curve. Two different SCRs interacting with three different shear strengths of seabed soils have been studied when they are forced to have a periodic heave or surge at their upper end. The trenching development at the seabed and the maximum variation in bending moment near their TDZ are estimated as function of time lapse after they start experiencing cyclic loading. The results show that a trench gradually deepened at the seabed may smooth curvature of risers near their TDZ

and in turn the maximum (spatial) change rate of bending moment near the TDZ. Our simulation indicates the maximum variation of bending moment near the TDZ mainly depends on the maximum (spatial) change rate of bending moment near the TDZ and the excursion of the TDP due to the heave or surge at the upper end of the riser. Since the excursion of the TDP does not change substantially with or without trenching, the reduced maximum (spatial) change rate of bending moment near the TDZ is responsible for the decrease in maximum variation in the bending moment near TDZ. This finding is consistent with the decrease in the maximum change rate of bending moment near the TDZ when the computation was conducted based on a static riser and a trench at the seabed prescribed empirically (Hahn et al, 2003). The reduction in the maximum variation of the bending moment results in the reduction in the stress level of a riser near the TDZ, which increases the allowable loading cycles, namely, its fatigue life. Our simulation indicates the relative reduction in the maximum variation of the bending moment is greater when the amplitude of heave or surge is smaller and/or seabed soil has lower shear strength. Since a deep-water floating structure experiences oscillations of small amplitudes during most time of its life span, this finding is relevant to the estimate the fatigue life of SCRs. For example, a 20% reduction in the maximum variation of bending moment near the TDZ may increase the estimated fatigue life by 100% near the TDZ.

Also the effects of two different types of upper end motions (surge and heave) on trenching behavior are studied. Our results indicate that for a similar amplitude, heave motion will result in a much larger trench than a surge motion. This is due to the fact that

the ratio of change in suspended length to motion is different for Heave and surge motion (Theckumpurath and Zhang, 2006).

In addition the relationship between wave period and trenching magnitude are discussed. The results show that a motion with smaller period will cause a larger trench. This is quite predictable since the smaller period (while the magnitude of the motion is constant) translates into higher velocities and acceleration and hence the bending moment and forces are increased.

It should be noted that the vortex induced vibration (VIV) and the lateral resistance experienced by risers in a trench at the seabed are neglected in our simulation. Furthermore, our simulation assumes periodic heave or surge at the upper end of a riser. Realistically, a SCR may experience non-periodic motions, such as irregular surge and sway in combination of heave at its upper end resulting from the motions of a floating structure. Therefore, our study should be further extended to allow for the factors mentioned above.

REFERENCES

American Petroleum Institute,. (2001). "Recommended practice for planning, designing and constructing fixed offshore Platforms - working stress design." API RP 2A-WSD, 21st Edition. API Publishing Services, Washington, D.C.

Aggarwal, R., Bhat, S., Meling, T., Mourelle, M., Linden, C., and Else, M. (2005). "Qualification of solutions for improving fatigue life at SCR touch down zone." Deep Offshore Technology Conference, Vitoria, Brazil.

Aubeny, C., Biscontin, G., and Zhang, J. (2006). "Seafloor interaction with steel catenary risers". Final report for MMS/OTRC project #1435-01-04-CA-35515. Offshore Technology Research Center, Texas A&M University, College Station.

Aubeny, C., and Biscontin, G. (2008). "Interaction model for steel compliant riser on soft seabed". OTC 194193, Houston, TX.

Aubeny, C., and Biscontin, G. (2009). "Seafloor-riser interaction model." *International Journal of Geomechanics,* 9, 133-141.

Bhat, J., Dutta, A., Wu, J., and Sarkar, I. (2004). "Pragmatic solution to touch-down zone fatigue challenges in steel catenary risers." OTC 16627, Houston, TX.

Bridge, C., Laver, K., Clukey, E., and Trevor, E. (2004). "Steel catenary riser touchdown point vertical interaction models." OTC 16628, Houston, TX.

Chen, X., Zhang J., Johnson, P., and Irani, M. (2001). "Dynamic analysis of mooring lines with inserted springs." *Applied Ocean Research,* 23, 277-284.

Chen, X. (2002). "Studies on dynamic interaction between deep-water floating structures and their mooring/tendon systems." Ph.D. Dissertation, Texas A&M University, College Station.

Clukey, E., Houstermans, L., and Dyvik, R., (2005). "Model tests to simulate riser-soil interaction in touchdown point region." *International Symposium on Frontiers in Offshore Geotechnics,* Center for Offshore Foundation Systems (COFS), Perth, Australia, 651-658.

Det Norske Veritas. (2006). "Offshore Standard DNV-OS-F105, Free spanning pipelines." DNV Services, Research and Publications, Hovik, Norway.

Det Norske Veritas. (2001). "Offshore Standard DNV-OS-F201, Dynamic risers." DNV Services, Research and Publications, Hovik, Norway.

Det Norske Veritas. (2005). "Recommended Practice DNV-RP-F204, Riser fatigue." DNV Services, Research and Publications, Hovik, Norway.

Dunlap, W., Bhohanala, R., and Morris, D. (1990). "Burial of vertically loaded offshore pipelines." OTC 6375, Houston, TX.

Giertsen, E., Verley, R., and Schroder, K. (2004). "CARISMA: a catenary riser/soil interaction model for global riser analysis." OMAE 51345, Vancouver, Canada.

Hahn, G.D., Shanks, J.M., and Masson, C. (2003). "An assessment of steel catenary riser trenching." Deep Offshore Technology International Conference, Marseille, France.

Health and Safety Executive. (1999). "Offshore Technology Report OTO-1999-058: Fatigue design curves for welded joints in air and seawater under variable amplitude loading." HSE Publications, London, UK.

Idriss, I.M., Dobry, R., and Singh, R.D. (1978). Nonlinear behavior of soft clays during cyclic loading." *Journal of Geotechnical Engineering*, 104 (12), 1427-1447.

Jiao, Y., (2007). "Non-linear load-deflection models for seabed interaction with steel catenary risers." M.S. Thesis, Texas A&M University, College Station.

Leira, B., Passano, E., Karunakaran, D., Farnes, K., and Giertsen, E. (2004). "Analysis guidelines and application of a riser-soil interaction model including trench effects." OMAE 51527, Vancouver, Canada.

Ma, W., and Webster, W.C. (1994). "An analytical approach to cable dynamics: theory and user manual." SEA GRANT Project R/OE-26. California University, Berkeley, CA.

Nakhaee, A., and Zhang, J. (2007). "Dynamic interaction between SCR and the seabed." OMAE Conference, San Diego, CA.

Nakhaee, A., and Zhang, J. (2008). "Effects of the interaction with the seabed on the fatigue life of a SCR." ISOPE Conference, Vancouver, Canada.

Pesce, C., Martins, C., and Silveira, L. (2006). "Riser-soil interaction: local dynamics at TDP and a discussion on the eigenvalue and the VIV problems." *Journal of Offshore Mechanics and Arctic Engineering,* 128, 39-55.

Theckumpurath, B., and Zhang, J. (2006). "Numerical simulation of the truss spar Horn Mountain." *Proceedings of the 16th ISOPEC*, ISOPE I, 196-203.

Thethi, R., and Moros, T. (2001). "Soil interaction effects on simple catenary riser response." Deepwater Pipeline and Riser Technology Conference, Houston, TX.

Willis, N.R.T., and West, P.T.J. (2001). "Interaction between deepwater catenary risers and a soft seabed: large scale sea trials." OTC 13113, Houston, TX.

Xu, J., Jesudasen, A.S., Fang, J., and Else, M. (2006). "Wave loading fatigue performance of SCRs in underwater applications." OTC 18180, Houston, TX.

APPENDIX A

NON-DEGRADATION SOIL MODEL

```matlab
% Non degradation P-y curve based on Dr Aubeny's model (Jiao, 2007)
% Ali Nakhaee

clc
close all;
clear all;

% INPUT

a=fopen('input.txt','r');
su0=fcanf(a,'%g',1);                     % Soil shear strength
sug=fcanf(a,'%g',1);                     % Gradient of soil shear
strength
Er=fscanf(a,'%g',1);
t=fcanf(a,'%g',inf);                     % Thickness of SCR
d=fcanf(a,'%g',inf);                     % External diameter of SCR
rho_steel=fcanf(a,'%g',1);               % Density of steel

% Model parameters

a1=fcanf(a,'%g',1);
b1=fcanf(a,'%g',1);
a2=fcanf(a,'%g',1);
b2=fcanf(a,'%g',1);
k=fcanf(a,'%g',1);
phi=fcanf(a,'%g',1);
psi=fcanf(a,'%g',1);
omega=fcanf(a,'%g',1);

fclose(a);

%%

Area=pi*(d-t)*t;                         % Cress sectional area of SCR
w=Area*rho_steel                         % unit weight of SCR

% Backbone curve

y(1)=0;
p(1)=0;
err2=-1;
ib=1;
while(err2<=0)
    y(ib+1)=y(ib)+0.002;
    if y(ib+1)/d<0.52;
        a=a1;
        b=b1;
    else
        a=a2;
        b=b2;
    end
    p(ib+1)=a*(y(ib+1)/d)^b*(su0+sg*y(ib+1))*d;
```

```matlab
    err2=P(ib+1)-w;
ib=ib+1;
end

yy1=y(ib)-.002;
PP1=a*(yy1/d)^b*(Su0+Sg*yy1)*d;
y1=yy1;
P1=PP1;
Prup=-phi*P1;
Y=y1;
y_1=y1;
alpha=0.016;
beta=0.0016;
k0=k_normal*Er*(Su0+Sg*yy1);

b=fopen('yhistory.txt','r');
yhist=fscanf(b,'%g',inf);
fclose(b);
ylength2=size(yhist);
yy=[y(1:ib-1) yhist'];

% unloading and reloading

ul0=-1;
yold=y1;
Pold=P1;
ib=ib-1;
Prev=P1;
yrev=y1;

AA=0;

for i=1:ylength2
    ynew=y(ib+1);
    ul=(ynew-yold)/abs(ynew-yold);
    [P2 y2 y3]=f(y1,P1,k0,phi,psi,omiga);

    if ynew<=y3||i==1
        yrc=y3;
        Prc=0;
    end

    if ul~=ul0
        Prev=Pold;
        yrev=yold;
        ul0=ul;
    end

    dy=ynew-yrev;

    AA=AA+dy*pold
```

```
if ul==-1

    if ynew>y2
        Pnew=Prev+(dy/((1/k0)+ul*dy/((1+omega)*P1)));

        if Pnew<=bound1(ynew,y1,P1,k0,omega)
            Pnew=bound1(ynew,y1,P1,k0,omega);
        end

    elseif ynew>y3
        Pnew=Prev+(dy/((1/k0)+ul*dy/((1+omega)*P1)));

        if Pnew<=bound2(ynew,y2,y3,P2)
            Pnew=bound2(ynew,y2,y3,P2);
        end

    else
            Pnew=0;
    end

elseif ul==1

    if ynew>y1
        Pnew=a*(ynew/d)^b*(Su0+Sg*ynew)*d;
        P1=Pnew;
        y1=ynew;
        Prup=-phi*P1;
        [P2,y2,y3]=f(y1,P1,k0,phi,psi,omega);

        elseif ynew>y3

            if yrev<=y1&&yrev>=y2
                Pnew=Prev+(dy/((1/k0)+ul*dy/((1+omega)*P1)));

            else
                Pnew=Prev+(dy/((1/k0)+ul*dy/((1+omega)*P1)));

                if Prev==bound2(yrev,y2,y3,P2)
                    yrc=yrev;
                    Prc=Prev;
                    Pnew=bound3(ynew,y1,yrc,Prc,P1);
                end
            end

            if Pnew>=bound3(ynew,y1,yrc,Prc,P1)
                Pnew=bound3(ynew,y1,yrc,Prc,P1);
            end

        else
            Pnew=0;
```

```matlab
            end

    else
        disp('err11')
    end

    y(ib+1)=ynew;
    P(ib+1)=Pnew;
    yold=ynew;
    Pold=Pnew;
    ib=ib+1;
end

%

kk=(y2-y1)/(p2-p1);


output=[y;P];

c = fopen('output.txt', 'wt');
fprintf(c, 'y P\n');
fprintf(c, '%g %g\n ', output);
fclose(c)
```

APPENDIX B

DEGRADATION SOIL MODEL

```matlab
% Degradation P-y curve based on Dr Aubeny's model (Jiao, 2007)
% Includes trenching (permanant soil deformation)
% Ali Nakhaee

clc
close all;
clear all;

% INPUT

%
a=fopen('input.txt','r');
su0=fcanf(a,'%g',1);                    % Soil shear strength
sug=fcanf(a,'%g',1);                    % Gradient of soil shear
strength
Er=fscanf(a,'%g',1);
t=fcanf(a,'%g',inf);                    % Thickness of SCR
d=fcanf(a,'%g',inf);                    % External diameter of SCR
rho_steel=fcanf(a,'%g',1);              % Density of steel

% Model parameters

a1=fcanf(a,'%g',1);
b1=fcanf(a,'%g',1);
a2=fcanf(a,'%g',1);
b2=fcanf(a,'%g',1);
k=fcanf(a,'%g',1);
phi=fcanf(a,'%g',1);
psi=fcanf(a,'%g',1);
omega=fcanf(a,'%g',1);

alpha=fscanf(a,'%g',inf);               %cubic degradation control
parameter

fclose(a);

% Backbone curve

y(1)=0;
P(1)=0;
err2=-1;
ib=1;

while (err2<=0)
    y(ib+1)=y(ib)+.002;

    if y(ib+1)/d<0.52
        a=a1;
        b=b1;

    else
```

```matlab
        a=a2;
        b=b2;
    end


    P(ib+1)=a*(y(ib+1)/d)^b*(Su0+Sg*y(ib+1))*d;
    err2=P(ib+1)-w;
    ib=ib+1;
end

k0=k_normal*Er* (Su0+Sg*yy1);
yy1=y(ib)-.0001;
PP1=a*(yy1/d)^b*(Su0+Sg*yy1)*d;
y1=yy1;
P1=PP1;
Prup=-phi*P1;
Y=y1;
y_1=y1;



% Read loading history

b=fopen('yhistory.txt','r');
filetype=fscanf(b,'%g',1);

if filetype==1
    yhist=fscanf(b,'%g',inf);
    fclose(b);
    ylength2=size(yhist);
    yy=[y(1:ib-1) yhist'];

%

    ul0=-1;
    yold=y1;
    Pold=P1;
    ib=ib-1;
    Prev=P1;
    yrev=y1;

    for i=1:ylength2
        ynew=yy(ib+1);
        ul=(ynew-yold)/abs(ynew-yold);
        [P2 y2 y3]=f(y1,P1,k0,phi,psi,omega);

        if ynew<=y3||i==1
            yrc=y3;
            Prc=0;
        end

        if ul~=ul0
            Prev=Pold;
```

```
        yrev=yold;
        ul0=ul;
    end

    dy=ynew-yrev;
    Y=Y+abs(dy);
    y_1=yy1+eta*Y^0.5;
    P_1=a*(y_1/d)^b*(Su0+Sg*y_1)*d;

    if ul==-1

        if ynew>y2
            Pnew=Prev+(dy/((1/k0)+ul*dy/((1+omega)*P1)));

            if Pnew<=bound1(ynew,y_1,P_1,k0,omega)
                Pnew=bound1(ynew,y1,P1,k0,omega);
            end

        elseif ynew>y3
            Pnew=Prev+(dy/((1/k0)+ul*dy/((1+omiga)*P1)));

            if Pnew<=bound2(ynew,y2,y3,P2)
                Pnew=bound2(ynew,y2,y3,P2);
            end

        else
            Pnew=0;
        end

    elseif ul==1

        if ynew>y3
            xi=(y_1-yrev)/((P_1*(1+omega))*((y_1-yrev)/(P_1-
Prev)-1/k0));

            if yrev<=y1&&yrev>=y2

Pnew=Prev+(1/((1/(k0*dy))+ul/((1+omega)*P_1*xi)));

                if Pnew>=PP1
                    Pnew=PP1;
                    P1=PP1;
                    y1=ynew;
                    [P2,y2,y3]=f(y1,P1,k0,phi,psi,omega);
                end

            else

Pnew=Prev+(dy/((1/k0)+ul*dy/((1+omega)*P_1*xi)));

                if Prev==bound2(yrev,y2,y3,P2)
```

```
                              yrc=yrev;
                              Prc=Prev;
                              Pnew=bound3(ynew,y_1,yrc,Prc,P_1);
                      end

                      if Pnew>=PP1
                              Pnew=PP1;
                              y1=ynew;
                              [P2,y2,y3]=f(y1,P1,k0,phi,psi,omega);
                      end

                end

                if Pnew>=bound3(ynew,y_1,yrc,Prc,P_1)
                      Pnew=bound3(ynew,y_1,yrc,Prc,P_1);
                end

          else
                Pnew=0;
          end

          if ynew>=y_1
                Pnew=a*(ynew/d)^b*(Su0+Sg*ynew)*d-(P_1-PP1);
                P1=Pnew;
                P_1=2*Pnew-P_1;
          end

    else
          disp('err11')
    end

    y(ib+1)=ynew;
    P(ib+1)=Pnew;
    yold=ynew;
    Pold=Pnew;
    ib=ib+1;
end

elseif filetype==2
    NumCycle=fscanf(input,'%g',1);
    fclose(input);
    [P2 y2 y3]=f(y1,P1,k0,phi,psi,omega);

    if y3<0
          yend=-0.3*yy1;
          step=0.0001;
    else

          yend=0.8*yy1;
          step=0.0001;
```

```
        end


for N=1:NumCycle
    yhist=[y1-step:-step:yend,yend+step:step:10*y1];
    [ylength1,ylength2]=size(yhist);
    ul0=-1;
    yold=y1;
    Pold=P1;
    Prev=P1;
    yrev=y1;

    for i=1:ylength2
        ynew=yhist(i);
        ul=(ynew-yold)/abs(ynew-yold);
        [P2 y2 y3]=f(y1,P1,k0,phi,psi,omega);

        if ynew<=y3||i==1
            yrc=y3;
            Prc=0;
        end

        if ul~=ul0
            Prev=Pold;
            yrev=yold;
            ul0=ul;
        end

        dy=ynew-yrev;
        Y=Y+abs(dy);
        y_1=yy1+eta*Y^0.5;
        P_1=a*(y_1/d)^b*(Su0+Sg*y_1)*d;

        if ul==-1

            if ynew>y2
                Pnew=Prev+(dy/((1/k0)+ul*dy/((1+omega)*P1)));

                if Pnew<=bound1(ynew,y1,P1,k0,omega)
                    Pnew=bound1(ynew,y1,P1,k0,omega);
                end

            elseif ynew>y3

Pnew=Prev+(dy/((1/k0)+ul*dy/((1+omega)*P1)));

                    if Pnew<=bound2(ynew,y2,y3,P2)
                        Pnew=bound2(ynew,y2,y3,P2);
                    end

            else
```

```matlab
                            Pnew=0;
                        end

                    elseif ul==1

                        if ynew>y3

                            if yrev<y3
                                yrc=y3;
                                Prc=0;
                                Pnew=bound3(ynew,y_1,yrc,Prc,P_1);

                                    if Pnew>PP1
                                        Pnew=PP1;
                                        y1=ynew;

[P2,y2,y3]=f(y1,P1,k0,phi,psi,omega);


                                        break;

                                    end

                            end

                            if Pnew>=bound3(ynew,y_1,yrc,Prc,P_1)
                                Pnew=bound3(ynew,y_1,yrc,Prc,P_1);
                            end

                        else
                            Pnew=0;
                        end

                    else
                        disp('err11')
                    end

                    yn(i)=ynew;
                    PN(i)=Pnew;
                    yold=ynew;
                    Pold=Pnew;
                end

                y=[y,yn];
                P=[P,PN];
                y_peak(1,N)=y1;
                y_Peak=y_peak'/d;
                Yn(N,1)=Y'/d;
            end

    end
```

```
output=[y;P];
fid = fopen('output.txt', 'wt');
fprintf(fid, 'y P\n');
fprintf(fid, '%g %g\n ', output);
fclose(fid)
```

APPENDIX C

DEGRADATION SOIL MODEL WITH TRENCHING

```matlab
% Degradation P-y curve based on Dr Aubeny's model (Jiao, 2007)
% Includes trenching (permanant soil deformation)
% Ali Nakhaee

clc
close all;
clear all;

% INPUT

%
a=fopen('input.txt','r');
su0=fcanf(a,'%g',1);                    % Soil shear strength
sug=fcanf(a,'%g',1);                    % Gradient of soil shear
strength
Er=fscanf(a,'%g',1);
t=fcanf(a,'%g',inf);                    % Thickness of SCR
d=fcanf(a,'%g',inf);                    % External diameter of SCR
rho_steel=fcanf(a,'%g',1);              % Density of steel

% Model parameters

a1=fcanf(a,'%g',1);
b1=fcanf(a,'%g',1);
a2=fcanf(a,'%g',1);
b2=fcanf(a,'%g',1);
k=fcanf(a,'%g',1);
phi=fcanf(a,'%g',1);
psi=fcanf(a,'%g',1);
omega=fcanf(a,'%g',1);

alpha=fscanf(a,'%g',inf);               %cubic degradation control
parameter

fclose(a);

% SCR node data

r=fopen('scr.txt','r');
N=fcanf(r,'%g',1);                      % number of elements
p_i=fcanf(r,'%g',N);
x_i=fcanf(r,'%g',N);


for i=1:N

% Model parameters

    a1=fcanf(a,'%g',1);
    b1=fcanf(a,'%g',1);
    a2=fcanf(a,'%g',1);
```

```matlab
    b2=fcanf(a,'%g',1);
    k=fcanf(a,'%g',1);
    phi=fcanf(a,'%g',1);
    psi=fcanf(a,'%g',1);
    omega=fcanf(a,'%g',1);

    alpha=fscanf(a,'%g',inf);                    %cubic degradation control
parameter

    fclose(a);

% Backbone curve

    y(1)=0;
    P(1)=p_i(i);
    err2=-1;
    ib=1;

    while (err2<=0)
        y(ib+1)=y(ib)+.002;

        if y(ib+1)/d<0.52
            a=a1;
            b=b1;

        else
            a=a2;
            b=b2;
        end

        P(ib+1)=a*(y(ib+1)/d)^b*(Su0+Sg*y(ib+1))*d;
        err2=P(ib+1)-w;
        ib=ib+1;
    end

    k0=k_normal*Er* (Su0+Sg*yy1);
    yy1=y(ib)-.0001;
    PP1=a*(yy1/d)^b*(Su0+Sg*yy1)*d;
    y1=yy1;
    P1=PP1;
    Prup=-phi*P1;
    Y=y1;
    y_1=y1;


% Read loading history

    b=fopen('yhistory.txt','r');
    filetype=fscanf(b,'%g',1);

    if filetype==1
```

```matlab
        yhist=fscanf(b,'%g',inf);
        fclose(b);
        ylength2=size(yhist);
        yy=[y(1:ib-1) yhist'];

%

        ul0=-1;
        yold=y1;
        Pold=P1;
        ib=ib-1;
        Prev=P1;
        yrev=y1;

        for i=1:ylength2
            ynew=yy(ib+1);
            ul=(ynew-yold)/abs(ynew-yold);
            [P2 y2 y3]=f(y1,P1,k0,phi,psi,omega);

            if ynew<=y3||i==1
                yrc=y3;
                Prc=0;
            end

            if ul~=ul0
                Prev=Pold;
                yrev=yold;
                ul0=ul;
            end

            dy=ynew-yrev;
            Y=Y+abs(dy);
            y_1=yy1+eta*Y^0.5;
            P_1=a*(y_1/d)^b*(Su0+Sg*y_1)*d;

            if ul==-1

                if ynew>y2
                    Pnew=Prev+(dy/((1/k0)+ul*dy/((1+omega)*P1)));

                    if Pnew<=bound1(ynew,y_1,P_1,k0,omega)
                        Pnew=bound1(ynew,y1,P1,k0,omega);
                    end

                elseif ynew>y3
                    Pnew=Prev+(dy/((1/k0)+ul*dy/((1+omiga)*P1)));

                    if Pnew<=bound2(ynew,y2,y3,P2)
                        Pnew=bound2(ynew,y2,y3,P2);
                    end
```

```matlab
            else
                Pnew=0;
            end

        elseif ul==1

            if ynew>y3
                xi=(y_1-yrev)/((P_1*(1+omega))*((y_1-
yrev)/(P_1-Prev)-1/k0));

                if yrev<=y1&&yrev>=y2

Pnew=Prev+(1/((1/(k0*dy))+ul/((1+omega)*P_1*xi)));

                    if Pnew>=PP1
                        Pnew=PP1;
                        P1=PP1;
                        y1=ynew;
                        [P2,y2,y3]=f(y1,P1,k0,phi,psi,omega);
                    end

                else

Pnew=Prev+(dy/((1/k0)+ul*dy/((1+omega)*P_1*xi)));

                    if Prev==bound2(yrev,y2,y3,P2)
                        yrc=yrev;
                        Prc=Prev;
                        Pnew=bound3(ynew,y_1,yrc,Prc,P_1);
                    end

                    if Pnew>=PP1
                        Pnew=PP1;
                        y1=ynew;
                        [P2,y2,y3]=f(y1,P1,k0,phi,psi,omega);
                    end

                end

                if Pnew>=bound3(ynew,y_1,yrc,Prc,P_1)
                    Pnew=bound3(ynew,y_1,yrc,Prc,P_1);
                end

            else
                Pnew=0;
            end

            if ynew>=y_1
                Pnew=a*(ynew/d)^b*(Su0+Sg*ynew)*d-(P_1-PP1);
                P1=Pnew;
                P_1=2*Pnew-P_1;
```

```matlab
                end

        else
            disp('err11')
        end

        y(ib+1)=ynew;
        P(ib+1)=Pnew;
        yold=ynew;
        Pold=Pnew;
        ib=ib+1;
    end

elseif filetype==2
    NumCycle=fscanf(input,'%g',1);
    fclose(input);
    [P2 y2 y3]=f(y1,P1,k0,phi,psi,omega);

    if y3<0
        yend=-0.3*yy1;
        step=0.0001;
    else

        yend=0.8*yy1;
        step=0.0001;

    end


    for N=1:NumCycle
        yhist=[y1-step:-step:yend,yend+step:step:10*y1];
        [ylength1,ylength2]=size(yhist);
        ul0=-1;
        yold=y1;
        Pold=P1;
        Prev=P1;
        yrev=y1;

        for i=1:ylength2
            ynew=yhist(i);
            ul=(ynew-yold)/abs(ynew-yold);
            [P2 y2 y3]=f(y1,P1,k0,phi,psi,omega);

            if ynew<=y3||i==1
                yrc=y3;
                Prc=0;
            end

            if ul~=ul0
                Prev=Pold;
                yrev=yold;
```

```
                        ul0=ul;
                    end

                    dy=ynew-yrev;
                    Y=Y+abs(dy);
                    y_1=yy1+eta*Y^0.5;
                    P_1=a*(y_1/d)^b*(Su0+Sg*y_1)*d;

                    if ul==-1

                        if ynew>y2

    Pnew=Prev+(dy/((1/k0)+ul*dy/((1+omega)*P1)));

                            if Pnew<=bound1(ynew,y1,P1,k0,omega)
                                Pnew=bound1(ynew,y1,P1,k0,omega);
                            end

                        elseif ynew>y3

    Pnew=Prev+(dy/((1/k0)+ul*dy/((1+omega)*P1)));

                            if Pnew<=bound2(ynew,y2,y3,P2)
                                Pnew=bound2(ynew,y2,y3,P2);
                            end

                        else
                            Pnew=0;
                        end

                    elseif ul==1

                        if ynew>y3

                            if yrev<y3
                                yrc=y3;
                                Prc=0;
                                Pnew=bound3(ynew,y_1,yrc,Prc,P_1);

                                if Pnew>PP1
                                    Pnew=PP1;
                                    y1=ynew;

    [P2,y2,y3]=f(y1,P1,k0,phi,psi,omega);

                                    break;

                                end

                            end
```

```matlab
                                if Pnew>=bound3(ynew,y_1,yrc,Prc,P_1)
                                    Pnew=bound3(ynew,y_1,yrc,Prc,P_1);
                                end

                            else
                                Pnew=0;
                            end

                            yperm(i)=y3;

                        else
                            disp('err11')
                        end

                        yn(i)=ynew;
                        PN(i)=Pnew;
                        yold=ynew;
                        Pold=Pnew;
                    end

                    y=[y,yn];
                    P=[P,PN];
                    y_peak(1,N)=y1;
                    y_Peak=y_peak'/d;
                    Yn(N,1)=Y'/d;
                end

        end

end

% fit curve to permanant deformation

h=0.5;
ymax=max(yperm);
xnew=[];
ynew=[];
for i=1:N
    if yperm(i)>ymax*h;
        xnew=[xnew,x_i(i)];
        ynew=[ynew,yperm(i)];
    end
end

ylog=log(ynew);
xlog=xnew;
p=polyfit(xlog,ylog,2);
A2=p(1);
A1=p(2);
A0=p(3);
sigma=sqrt(-1/(2*A2));
mu=A1*sigma^2;
```

```
A=exp(A0+mu^2/(2*sigma^2));

y0_new=A*exp(-(x-mu).^2/(2*sigma^2));

output=[x_i;y0_new];

yy = fopen('output.txt', 'wt');

fprintf(fid, 'x_i y0_new\n');
fclose(fid)
```

VITA

Ali Nakhaee was born in Birjand, Iran in 1980. He received his Bachelor of Science degree in civil engineering from the University of Tehran in 2000. Two years later he received his Master of Science degree from the University of Tehran in civil engineering (marine structures). He entered the Ph.D. program in ocean engineering at Texas A&M University in January 2005 and graduated in December 2010. His research interests include numerical methods, fluid dynamics, and riser-soil interaction. He may be reached at Institute of Petroleum Engineering at University of Tehran, North Amirabad Av., Tehran, Iran. His email address is alinakhaee@yahoo.com.